2008

Integrated Optical Spr (surface Plasmon Resonance) Sensor Based On Optoelectronic Platform

Hyungseok Bang
University of Central Florida

INTEGRATED OPTICAL SPR (SURFACE PLASMON RESONANCE) SENSOR BASED ON OPTOELECTRONIC PLATFORM

by

HYUNGSEOK BANG
M.S. Korea University, 1998
B.S. Inha University, 1995

A dissertation submitted in partial fulfillment of the requirements
for the degree of Doctor of Philosophy
in the College of Optics and Photonics: CREOL and FPCE
at the University of Central Florida
Orlando, Florida

Summer Term
2008

Major Professor: Patrick LiKamWa

ABSTRACT

Current major demands in SPR sensor development are system miniaturization and throughput improvement. Structuring an array of integrated optical SPR sensor heads on a semiconductor based optoelectronic platform could be a promising solution for those issues, since integrated optical waveguides have highly miniaturized dimension and the optoelectronic platform enables on-chip optical-to-electrical signal conversion. Utilizing a semiconductor based platform to achieve optoelectronic functionality poses requirements to the senor head; the sensor head needs to have reasonably small size while it should have reasonable sensitivity and fabrication tolerance. This research proposes a novel type of SPR sensor head and demonstrates a fabricated device with an array of integrated optical SPR sensor heads endowed with optoelectronic functionality.

The novel integrated optical SPR sensor head relies on mode conversion efficiency for its operational principle. The beauty of this type of sensor head is it can produce clear contrast in SPR spectrum with a highly miniaturized and simple structure, in contrast to several-millimeter-scale conventional absorption type or interferometer type sensor heads.

The integrated optical SPR sensor with optoelectronic functionality has been realized by structuring a dielectric waveguide based SPR sensor head on a photodetector-integrated semiconductor substrate. A large number of unit sensors have been fabricated on a substrate with a batch fabrication process, which promises a high throughput SPR sensor system or low-priced disposable sensors.

ACKNOWLEDGMENTS

I appreciate Dr. Patrick LiKamWa and Dr. Hyoung Jin Cho for their support during the progress of my research and the development of dissertation. I would specially thank for giving me a freedom to explore diverse areas during the time in CREOL. From the experiences, I was able to acquire numerous skills and ideas.

I would also like to thank my dissertation committee for taking the time to review my dissertation. I would not forget the advice and the help of Dr. M. G. Moharam and Dr. Tae-Woo Lee regarding their theoretical support of my research also.

I am very thankful to colleagues and professors in CREOL and in Dept. of MMAE, especially the members of two groups that I belonged to (N. Bickel, P. Zhang, G. Londe, A. Wesser, E. Tafti, R. Shahbani, M. Montgomery, and T. Wang) for their warm hearted help.

Most importantly, I am grateful to my parents, my sister, and, specially, to my fiancée, who always be my best friend and a great supporter.

TABLE OF CONTENTS

LIST OF FIGURES

LIST OF TABLES

CHAPTER 1 INTRODUCTION

As life science attracts a great deal of attention and the application areas of biological technology have been broadened, the demand for more reliable and versatile biomolecule detection system has been emphasized. Ones of the most prominent types of biological agent sensing devices are affinity based biosensors. Affinity biosensors are composed of a biological recognition element, which is for recognizing target biological agent, and a transducer for converting achieved biological response into electrical signal. Diverse types of transducers have been developed for this purpose. Electrochemical, piezoelectric, and optical ways are some of the representative working methods for transducers [1-3]. Among them, optical methods, such as fluorescence spectroscopy, interferometry, evanescent wave based detection, and surface plasmon resonance (SPR) spectroscopy, have attracted great attention [4-8].

Traditionally, fluorescence based detection methods, such as ELISA (Enzyme-Linked ImmunoSorbent Assay), has long been used, due to its high sensitivity and high throughput characteristics [9, 10]. However, the detection process requires time-consuming labeling treatment and also is composed of multiple-steps of detection protocols. SPR based biomolecular detection technology was introduced rather recently. Detection protocols have been well developed and the detection systems have successfully been commercialized [11, 12]. This powerful technique does not require any kind of labeling steps and enables real-time monitoring, while offering high sensitivity. However most current commercial and developing level SPR sensors suffer from rather low throughput and relatively bulky system size [13, 14]. Those features limit the scope of SPR sensor's applications. Though some of the limitations have been partially resolved recently, there are still demands for higher throughput and more compact sized

SPR sensor systems [15, 16].

In this context, integrated optical SPR sensor based on optoelectronic platform has been suggested. An integrated optic system has several advantages for a biosensor platform [17, 18]. Firstly, the small size of waveguide based optical components enable significant reduction of entire sensor system. Secondly, high throughput sensor system can be achieved by integrating a large number of sensors on a substrate. Thirdly, through batch fabrication process, significantly reduced production cost can be achieved. Fourthly, since all the optical components are integrated on a single substrate, the sensor system is robust and stable. Finally, planar structure of the sensor platform provides the ideal environment for the integration of microfluidic channels, which are used for delivering liquid base specimens to the sensor heads [19-21].

In previous integrated optical SPR sensor research, only SPR sensor heads have been integrated on a substrate and the entire sensor systems have depended on bulk optical components for light generation and optical signal detection [20]. In this work, we propose a fully integrated SPR sensor scheme in which the SPR sensor head is integrated on an optoelectronic platform and demonstrate a prototype device.

CHAPTER 2 THEORETICAL BACKGROUND

2.1 Surface Plasmon Resonance (SPR)

Surface plasmon is a charge density wave propagating along a metal-dielectric interface. For surface plasmon to exist, the real part of the dielectric constant of the metal must be negative and its magnitude must be greater than that of the dielectric. The propagation constant of a surface plasmon is given by the following dispersion relation.

$$k_{sp}(\omega) = \frac{\omega}{c}\sqrt{\frac{\varepsilon_M \varepsilon_D}{\varepsilon_M + \varepsilon_D}} \tag{1}$$

2.2 Configurations for Surface Plasmon Excitation

Surface plasmons on a metal surface can be excited with a light if matching the wavevector of a surface plasmon and the tangential component of light's wavevector:

$$\beta(\omega) = k_{sp}(\omega) \tag{2}$$

However, propagating surface plasmons on a metallic surface cannot be excited by simply shining a beam of light on the surface, because surface plasmon's wavevector cannot be matched with light's wavevector in this condition. Therefore, a specially devised configuration, such as,

prism (Kretschmann configuration), grating, or optical waveguide is needed to satisfy wavevector matching condition [16].

2.2.1 Prism based surface plasmon excitation

Figure 2-1. shows a prism based configuration for surface plasmon excitation. This configuration utilizes the high refractive index of a prism for matching the wavevectors of a surface plasmon and a light beam. This configuration is also referred to as attenuated total reflection (ATR).

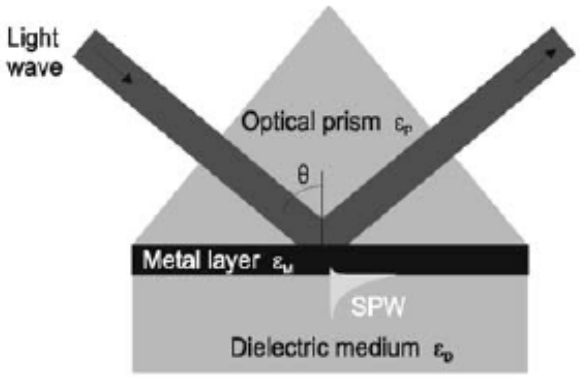

Anal Bioanal Chem (2003) 377: 528–539

Figure 2-1 Prism based surface plasmon excitation configuration (Kretschmann configuration)

In this configuration, light is introduced from a prism side and totally internally reflected (TIR) at the interface between the prism and the metal layer. The generated evanescent wave from TIR penetrates the metallic film and excites surface plasmons on the other side of the metal layer. Figure 2-2 shows dispersion curves of light in the dielectric medium, prism, and surface plasmon.

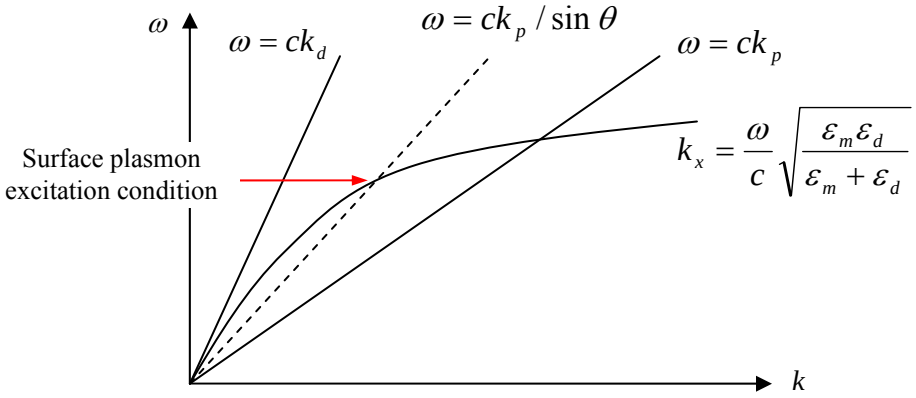

Figure 2-2 Dispersion curves of surface plasmon and the light in the dielectric medium and prism

As the figure shows, the dispersion curves of surface plasmon and light can be matched with the help of high refractive index prism. The wavevector matching condition is usually achieved by adjusting the incident angle of the optical beam.

2.2.2 Grating based surface plasmon excitation

Using a grating is another way of compensating wavevector mismatch, as represented in Figure 2-3. In the case of grating coupled surface plasmon excitation, light is directly incident on the grating patterned metallic surface. In this configuration, wavevector matching condition is assisted by the wavevector of the grating.

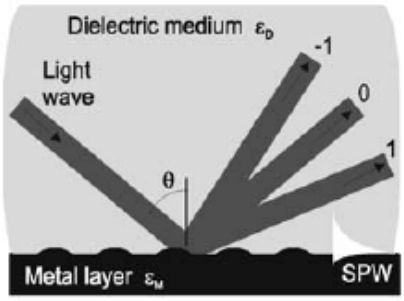

Anal Bioanal Chem (2003) 377: 528–539

Figure 2-3 Grating based surface plasmon excitation configuration

Equation 3. represents the surface plasmon excitation condition with the help of grating's wavevector addition or subtraction.

$$k_{sp} = \pm n \cdot k_{grating} + k_{light,\,\text{tan}\,gential} \tag{3}$$

$$k_{light,\,\text{tan}\,gential} = \sqrt{\varepsilon_d} \cdot k_0 \cdot \sin\theta \tag{4}$$

Figure 2-4. schematically explains the excitation conditions of surface plasmon. Surface plasmon can be excited when the dispersion curves match.

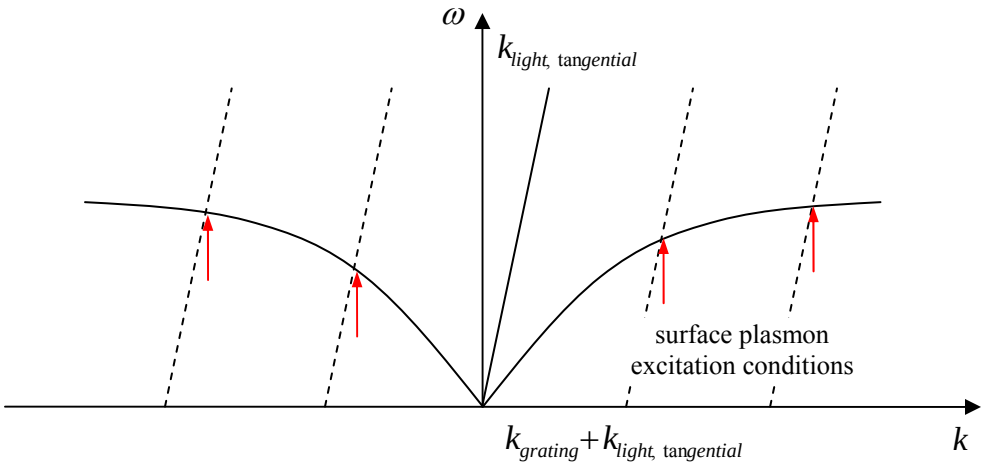

Figure 2-4 Dispersion curves of surface plasmon and light's dispersion curve modulated by a grating

2.2.3 Optical waveguide based surface plasmon excitation

Surface plasmon resonance condition can also be achieved by matching the wavevectors of a guided mode with that of a surface plasmon. As it does in prism coupling configuration, the evanescent field penetrates the metal film and excites surface plasmons on the opposite side of the metal film, as demonstrated in Figure 2-5.

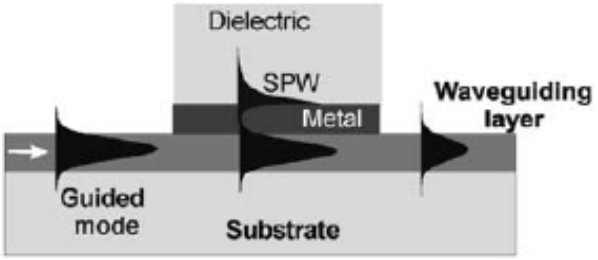

Anal Bioanal Chem (2003) 377: 528–539

Figure 2-5 Optical waveguide based surface plasmon excitation configuration

When the wavevector matching condition is satisfied, the resonance between surface plasmon and waveguiding mode happens. In this condition the energy of the light is transferred to the surface plasmon and the intensity of the light in the guided mode is significantly attenuated at the resonance frequency.

2.3 Principles of SPR based Biomolecular Detection

The dispersion characteristics of surface plasmons are extremely sensitive to the refractive index of dielectric material which is in contact with a metal surface. And this refractive index sensitive characteristic of surface plasmons is used for biomolecular detection [22].

2.3.1 Biomolecular binding and SPR spectrum

Basically a SPR sensor is a very sensitive refractometer, which can read the refractive index variation when biomolecular binding happens. As described in Figure 2-6, when analyte molecules bind to biomolecule recognition elements, which are immobilized on a SPR sensor head, slight refractive index rise happens on the layer of recognition elements. The increased refractive index, in turn, changes the resonance frequency of surface plasmons on the metal-analyte boundary. In the case of spectral type SPR sensor, the changed refractive index is evidence by a shift of the position of the resonance in the SPR spectrum.

The increase of refractive index depends on the number of bound analyte molecules to the biomolecule recognition elements. The frequency shift can be monitored using diverse configurations. The monitoring is performed by interrogating reflected or transmitted light from the sensor head. Reflected light intensity distribution and transmitted light spectrum reflects the number of molecules bound to the sensor head.

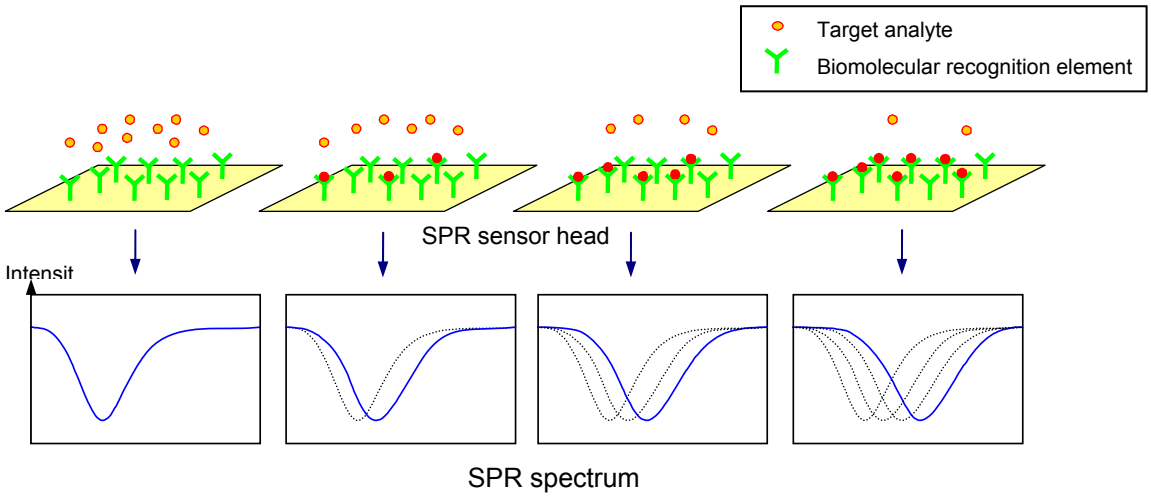

Figure 2-6 Biomolecular binding and SPR spectrums

2.3.2 SPR Sensorgram

A SPR sensorgram indicates the association and dissociation conditions of analyte molecules on the sensor head. Overall concentration and the kinetics of biomolecular interaction can be determined from the shape and amplitude of SPR sensorgram. Figure 2-7. demonstrates an example of SPR sensorgram.

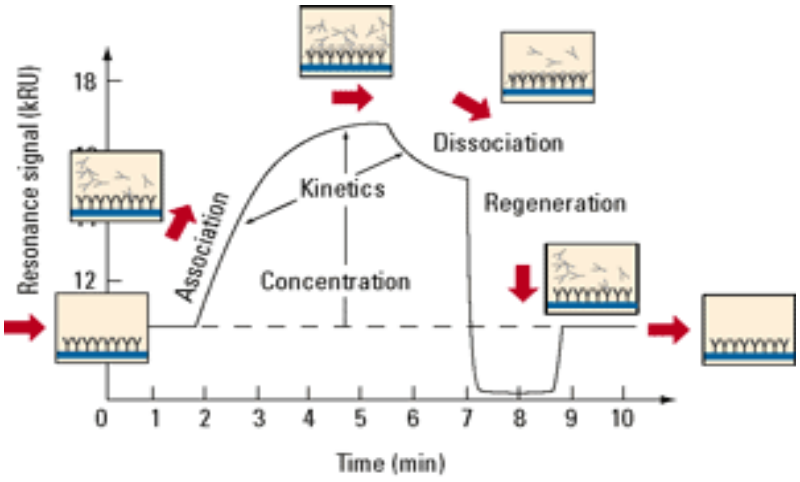

Courtesy of Biacore International AB

Figure 2-7 SPR sensorgram

CHAPTER 3 PREVIOUS WORKS

3.1 SPR Imaging Sensor

To achieve a high throughput system, there has been an approach of multichannel SPR sensing using a prism with an array of SPR sensor heads on it. SPR imaging is a type of intensity modulation based detection by directing a collimated beam of monochromatic light to the arrayed sensor head with a lens system and imaging the reflected beam to a detector array. Figure 3 demonstrates a schematic view of a SPR imaging system, which was reported by Homola et al. in 2005.

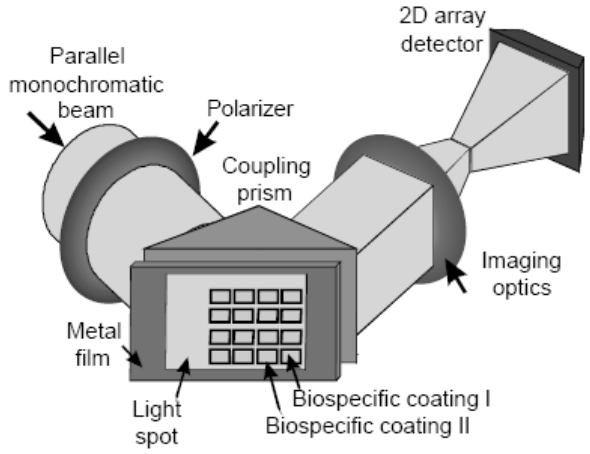

Figure 3-1 SPR imaging sensor

This configuration contains $3x10^{-6}$ RIU of good resolution and has the capability to simultaneously process 100 samples. Along with arrayed integrated optical SPR sensors, this system is also promising in achieving high throughput sensor systems.

3.2 Integrated Optical SPR Sensor

As described earlier, integrated optical SPR sensors have significant importance in the respect of system miniaturization and throughput improvement. The integrated optical SPR sensors that have been studied up to now, can be categorized into three main types; absorption type, interferometer type, and mode transition type.

3.2.1 Absorption type integrated optical SPR sensor

Absorption type integrated optical SPR sensors have been the most widely studied among integrated optical waveguide type SPR sensors. Absorption type SPR sensors rely on energy transfer from dielectric waveguide to metal layer in acquiring SPR spectrum. When the wavevector of guided mode satisfy the resonance condition the energy in dielectric region transfers to surface plasmons on the metal layer. As for the sensor head structure, single mode dielectric waveguides were used and a thin layer of gold was deposited to form a SPR sensor head. In most of the waveguide fabrication process, ion exchanged glass waveguides were used.
The experiment for SPR spectrum acquisition was performed by launching a polychromatic light to the sensor head or launching a monochromatic light and scanning the wavelength with a tunable laser.

3. 2.1.1 Polychromatic light launching method

White light launching and spectrum achieving method has been widely used for integrated optical SPR sensing configurations. As described in Fig. 3-2, this method launches all the spectrum of light into a sensor head and observes the modulated spectrum with a spectrometer.

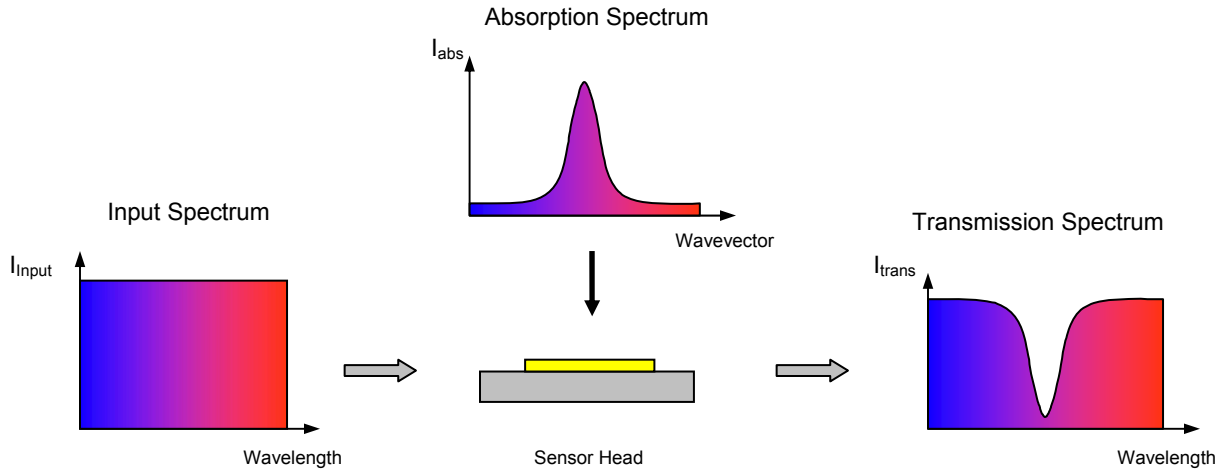

Figure 3-2 White light launching and spectrum achieving method

Dostalek et al. (in 2001) have used a broadband light source for acquiring the SPR spectrum [20]. Figure 3-3 display integrated optical SPR sensors developed by Dostalek et al. The dielectric waveguides were fabricated by $K^+ \leftrightarrow Na^+$ ion exchange process performed on a glass.

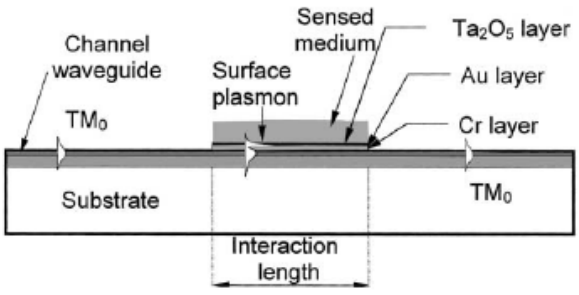

Figure 3-3 Integrated optical SPR sensor developed by Dostalek et al.

Figure 3-4 demonstrates a SPR experimental set up developed by Wang et al. A broadband light source was used as a polychromatic light source and a modulated spectrum of the light from the sensor head was captured by a spectrometer.

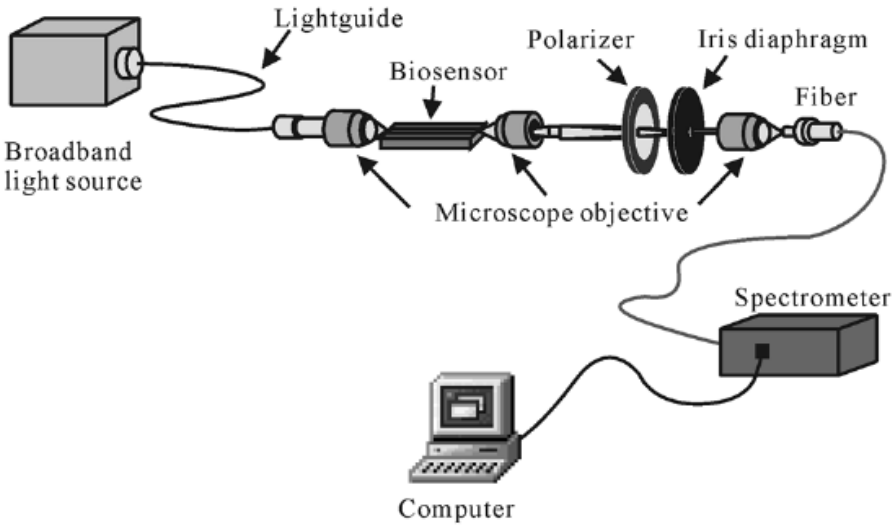

Figure 3-4 SPR experimental set up based on a polychromatic light source and a spectrometer

A SPR experimental set up with a polychromatic light source and a spectrometer has the capability to acquire a spectrum in a swift way. However, in the respect of developing all-integrated sensor system, this scheme is not practical, because of the difficulty in micro-scale fabrication of the spectrometer.

3. 2.1.2 Monochromatic light launching and spectrum scanning method

A SPR spectrum can also be achieved by launching a monochromatic light and modulating the wavevector of the guided mode in the sensor head. The wavevector of the guided mode can be modulated by changing the wavelength of launched light or by changing the refractive index of the waveguide material.

i) Wavelength modulation method

Wavelength modulation method launches a light from a wavelength tunable light source into a sensor head and scans the wavelength in a range [24]. The modulation of wavelength directly affects to the wavevector of a guided mode. Fig. 3-6 shows SPR spectrum acquirement process using the wavelength modulation method.

In 1997, Ctyroky et al. have developed an integrated optical SPR sensor and a wavelength modulation type experimental set up. Figure 3-6 and Figure 3-7 demonstrate an integrated optical SPR sensor for wavelength modulation SPR experiment and a SPR spectrum achieved from the device.

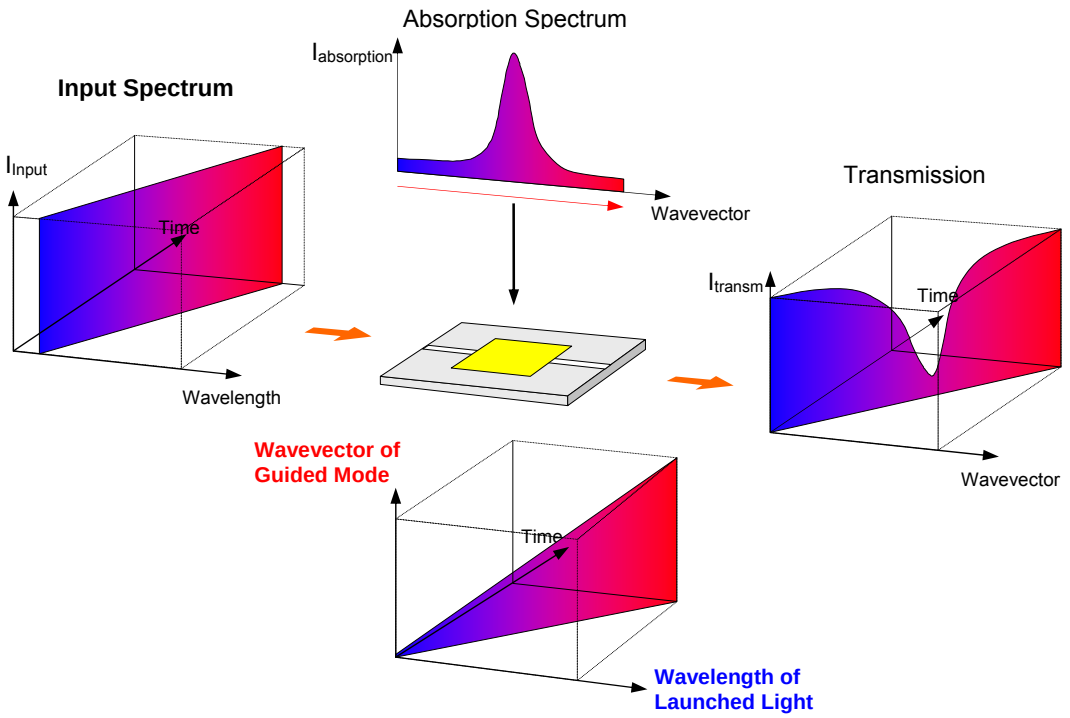

Figure 3-5 Wavelength modulation based SPR spectrum acquisition

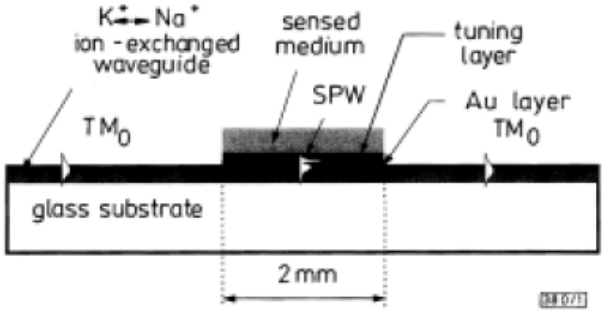

Figure 3-6 Integrated optical SPR senor for wavelength modulation SPR experiment

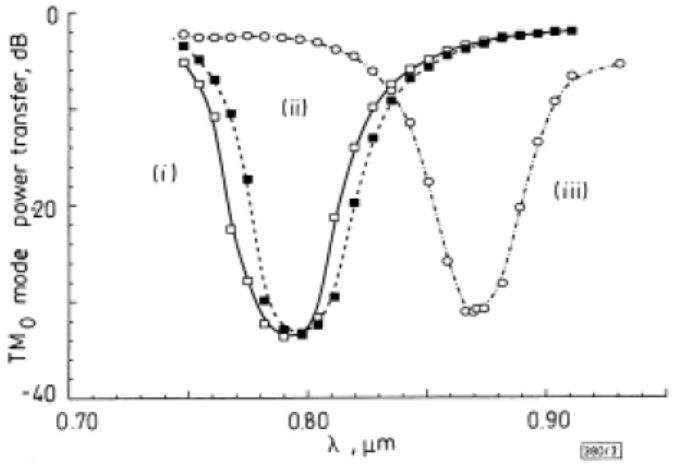

Figure 3-7 SPR spectrum achieved form the wavelength modulation experiment

ii) Waveguide refractive index modulation

In this method, a light with fixed wavelength is launched into the waveguide of a sensor head and the refractive index of the waveguide is modulated. As the waveguide material's refractive index changes, the wavevector of a guided mode also changes. Surface plasmon excitation happens, when the wavevector of guided mode matches with the wavevector of a surface plasmon, which will result in energy transfer from dielectric guided mode to surface plasmons. Fig. 3-8 shows the SPR spectrum acquirement process by waveguide refractive index modulation method.

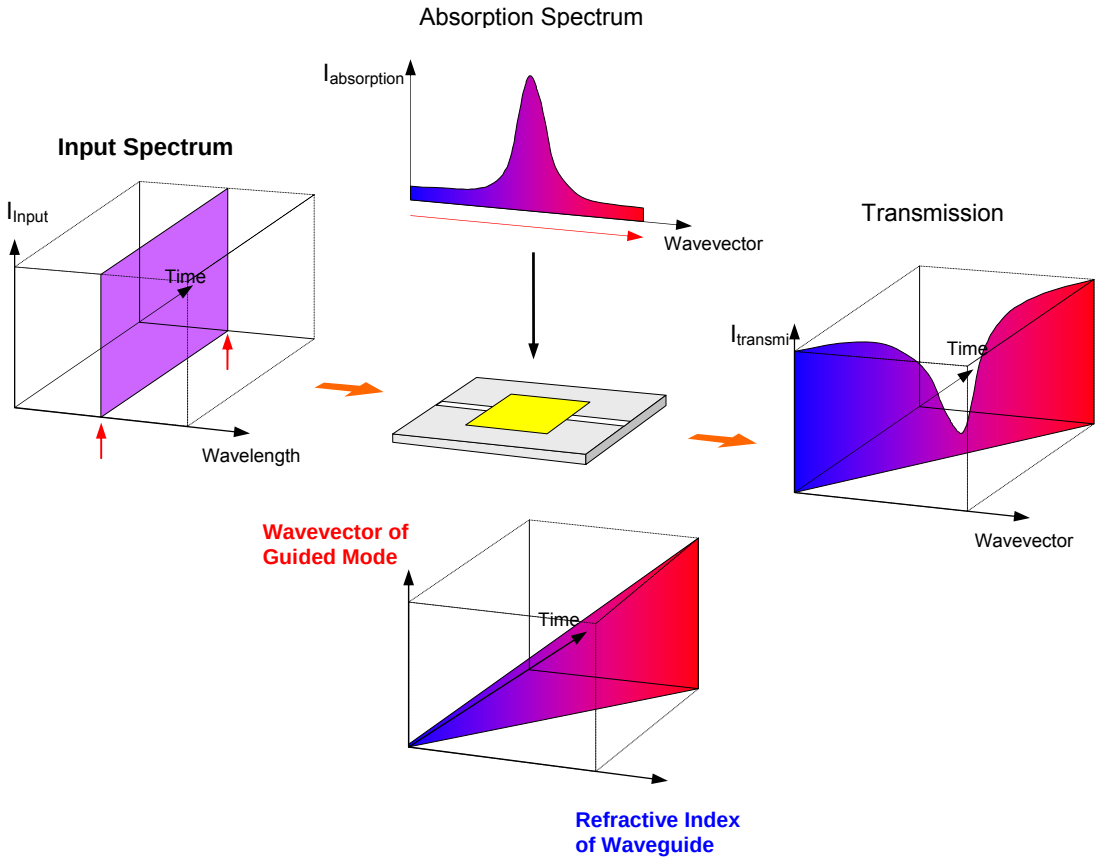

Figure 3-8 Waveguide refractive index modulation based SPR spectrum acquisition

Fig. 3-9 shows the sensor reported by Wang et al. in 2007 [23]. In this work, titanium diffused lithium niobate substrate was used as an optical waveguide to utilize the electro-optic properties of $LiNbO_3$ substrate. The refractive index control for the variation of the guided mode's wave vector was exercised by applying electric voltage to the sensing waveguide. Figure 3-10 shows dependence of the SPR wavelength on the applied voltage for different analyte molecules.

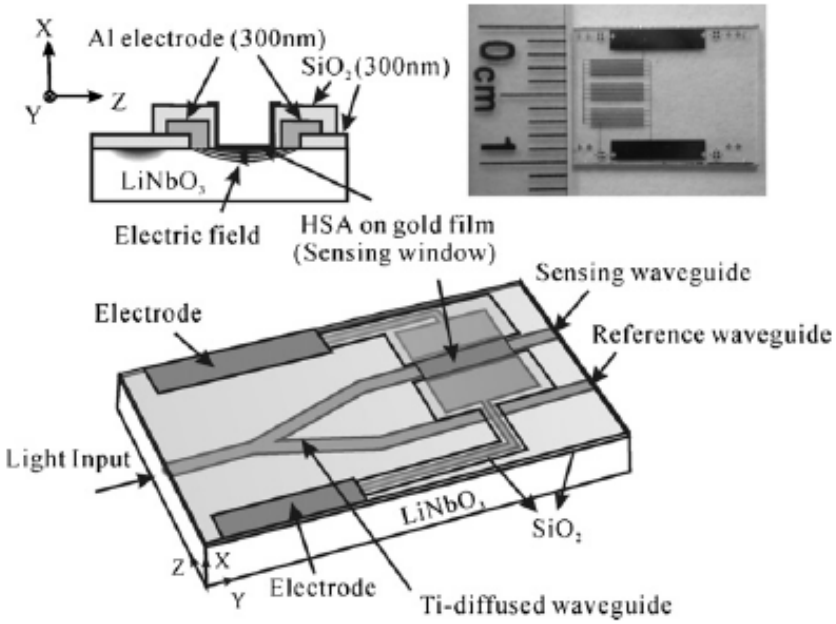

Figure 3-9 Integrated optical SPR sensor with electro-optic modulation method

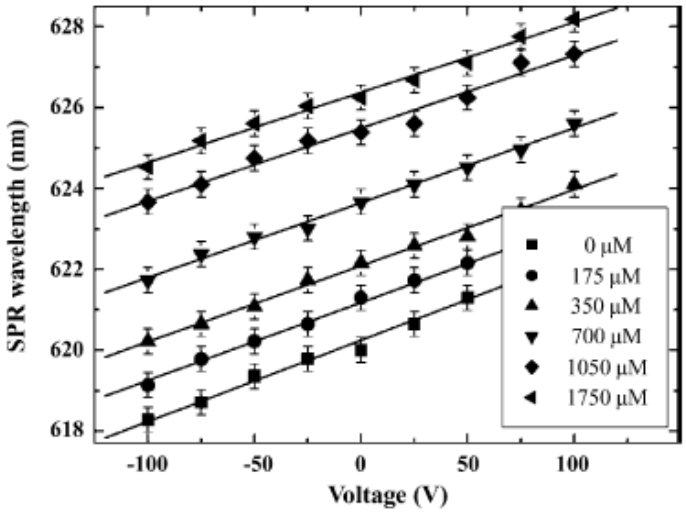

Figure 3-10 Dependence of the SPR wavelength on the applied voltage for different beta-blocker concentrations (0–1750_M)

However, the voltage range required to cover entire scan range was rather large. To cover surface plasmon wavelength from 618 to 628 nm, the voltage has to be changed from -100 to +100 volts, which is relatively large for portable equipments considering the voltages generated from conventional hand-held batteries. Also there can be a difficulty in achieving the capability of on-substrate light generation and optical to electrical conversion with lithium niobate substrate.

3. 2.2 Interferometer type integrated optical SPR sensor

Most of studies on interferometer type integrated optical SPR sensors have been performed by theoretical simulations. Generally, conventional Mach-Zehnder interferometer (MZI) SPR sensors with branched arms have been most studied.

In 2006, P. Debackere et al. reported their research on silicon-on-insulator (SOI) based MZI SPR sensor scheme. Figure 3-11 demonstrates the silicon-on-insulator based SPR sensor head. In this scheme, a mode guided in the silicon waveguide excites the surface plasmons on both the top and bottom sides of the gold layer, using end fire coupling technique. The excited top and bottom surface plasmons propagate along the gold layer covered sensor head and re-excite a guided mode in a silicon waveguide. Depending on phase of the surface plasmons at the end of the sensor head, the plasmons will either constructively or destructively interfere, which in turn define the output power. Figure 3-12 shows the transmission spectrum from the structure as a function of superstrate refractive index from the simulation.

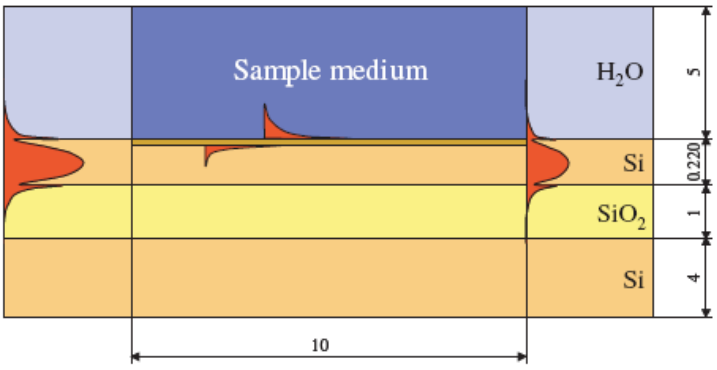

Figure 3-11 Schematic of SOI based SPR sensor head (dimensions in um)

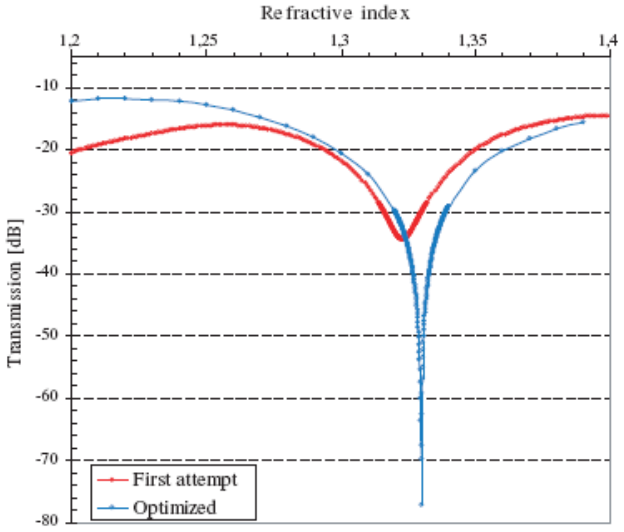

Figure 3-12 Transmission as a function of Refractive index

However, this scheme requires stringently tight fabrication tolerance to achieve comparable intensities of surface plasmons on both layers. According to the report made in Proc. of SPIE Vol. 6477 (2007) by P. Debackere et al., the experimental results indicate that the device is functioning properly but qualitative agreement between theoretical and experimental results had not been achieved yet. Figure 3-13 the image of a fabricated SOI based SPR device. by P. Debackere et al.

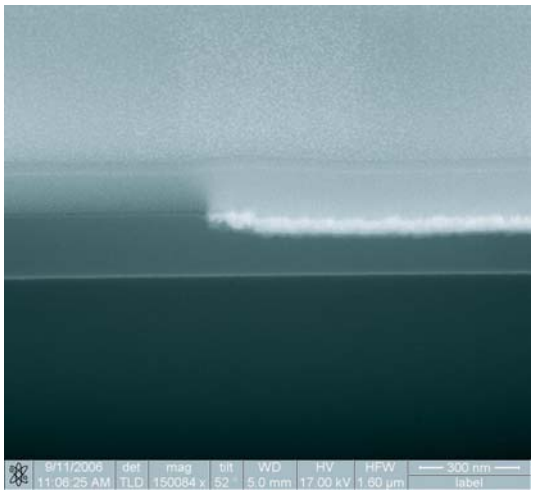

Figure 3-13 Cross-section image of a fabricated SOI based SPR device

CHAPTER 4 INTEGRATED OPTICAL SPR SENSOR BASED ON MODE CONVERSION EFFICIENCY

4.1 Waveguide Geometry and Supported Eigen Modes

For the waveguide geometry, an inverted rib type waveguide was designed that can only support the fundamental TM mode and it forms the back bone of the sensor, as shown in Figure 4-1. A portion of the waveguide covered with a thin gold layer forms SPR sensor head. The gold covered region supports two bound eigen modes, which were termed as SPD-S mode and SPD-A mode respectively. The SPD-S and SPD-A modes are the combined fields of a surface plasmon polariton (SPP) and a dielectric guide wave (DGW) modes.

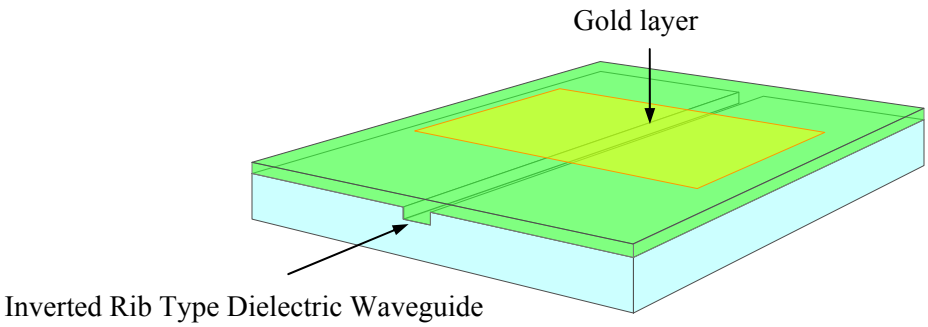

Figure 4-1 Configuration of mode conversion efficiency type SPR sensor head

Figure 4-2 (a) and (b) show the characteristic field profile of a SPD-S mode. As shown in the figures, the SPD-S mode has the same field directions on the gold and in the dielectric waveguide region. SPD-S mode is a purely bound mode.

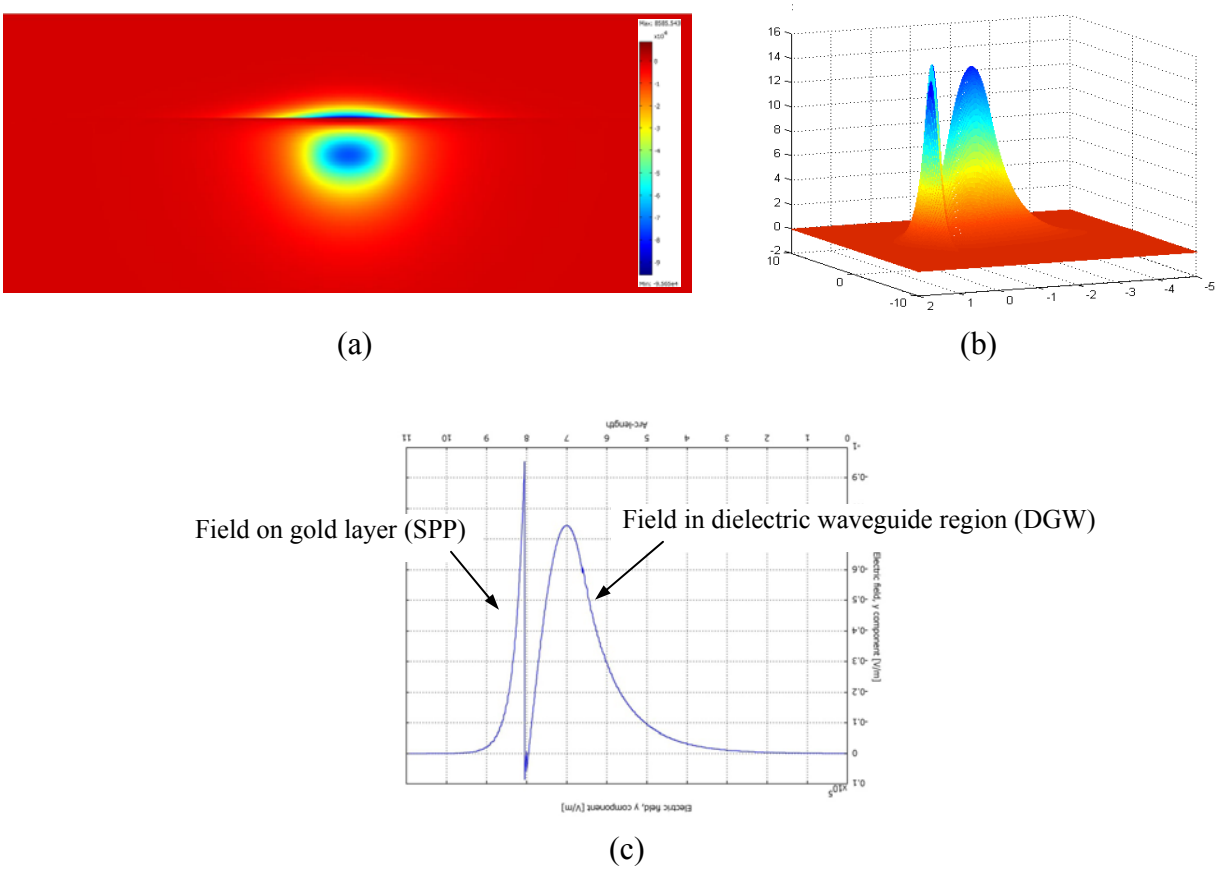

Figure 4-2 SPD-S mode filed profile

(a) Front view, (b) 3-dimensional view, and (c) 2-dimensional view

Figure 4-3 (a) and (b) show the characteristic field profile of a SPD-A mode. The SPD-A mode shows a field direction on the gold layer that is opposite to that in the dielectric waveguide region. In fact the SPD-A mode is a quasi bound mode.

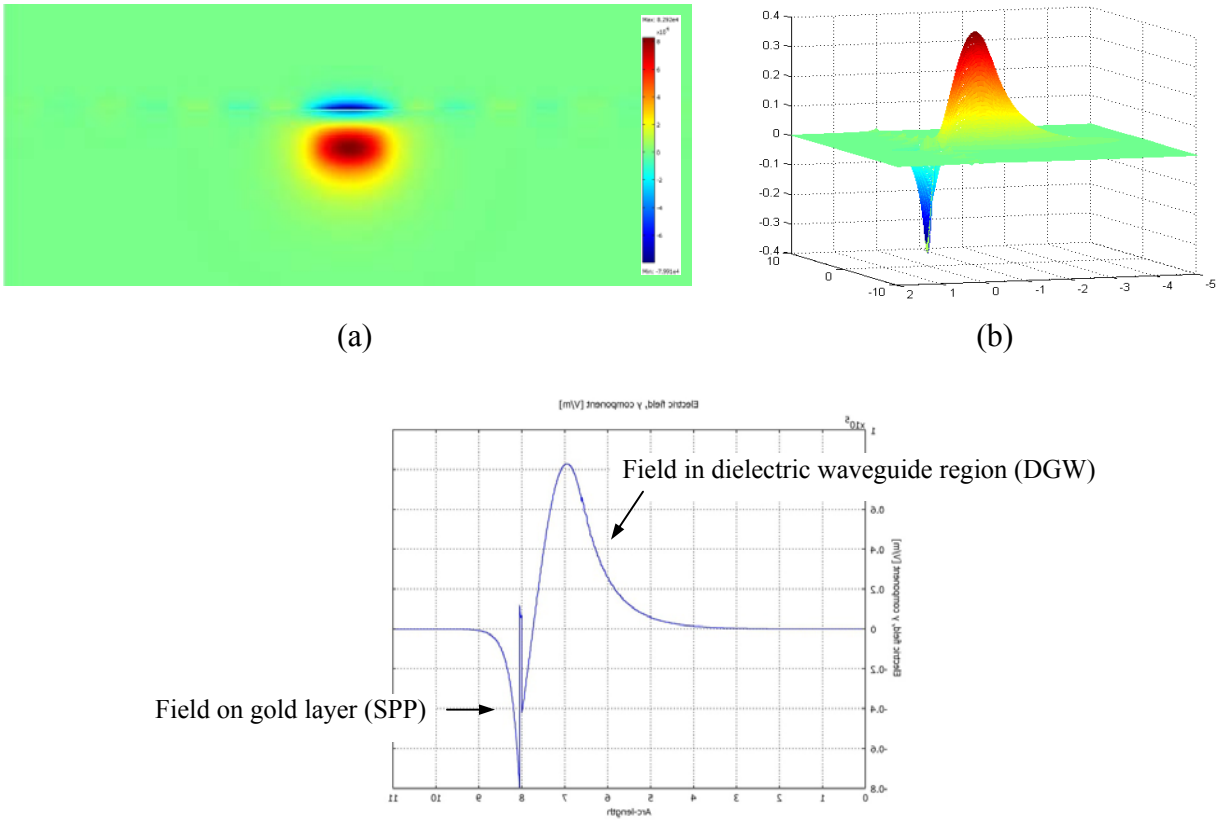

Figure 4-3 SPD-A mode filed profile

(a) Front view, (b) 3-dimensional view, and (c) 2-dimensional view

There are many other leaky modes in addition to the above bound and quasi bound modes. Figure 4-4 (a), (b), and (c) show a contour plot, a 3-dimensional field, and a 2-dimensional graph of a representative leaky mode.

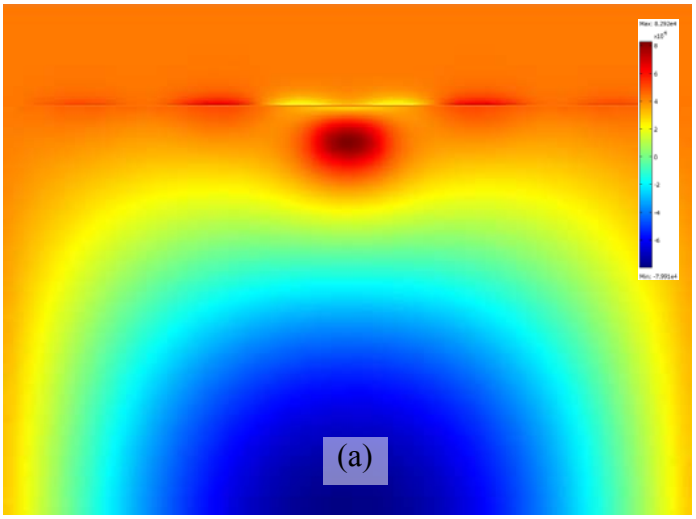

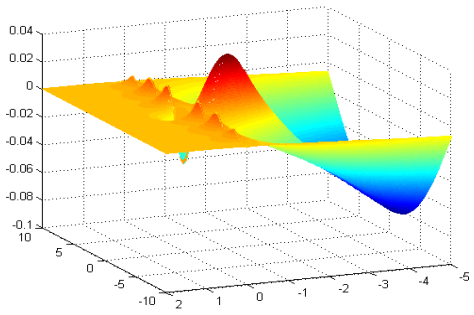

(b)

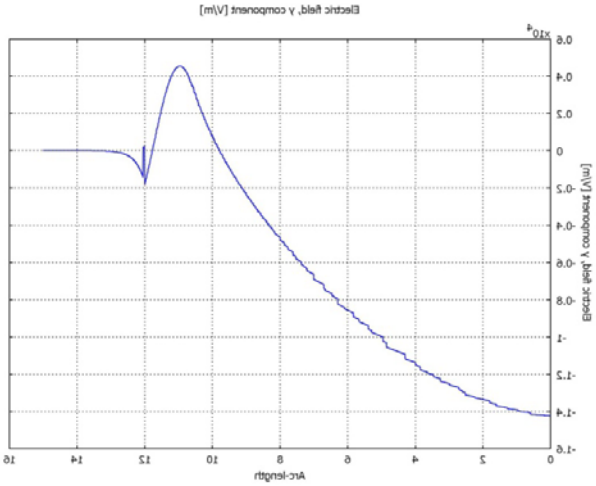

(c)

Figure 4-4 Leaky mode filed profile

(a) Front view, (b) 3-dimensional view, and (c) 2-dimensional view

4.2 Mode Profile Spectral Dependence

The wavelength dependences of the field profiles of the SPD-S and SPD-A modes are shown in figure 4-5. In a long wavelength range, from 750 nm to 800 nm, only SPD-S mode exists. In the short wavelength range, from 680 nm to 740 nm, both the SPD-S and SPD-A modes co-exist.

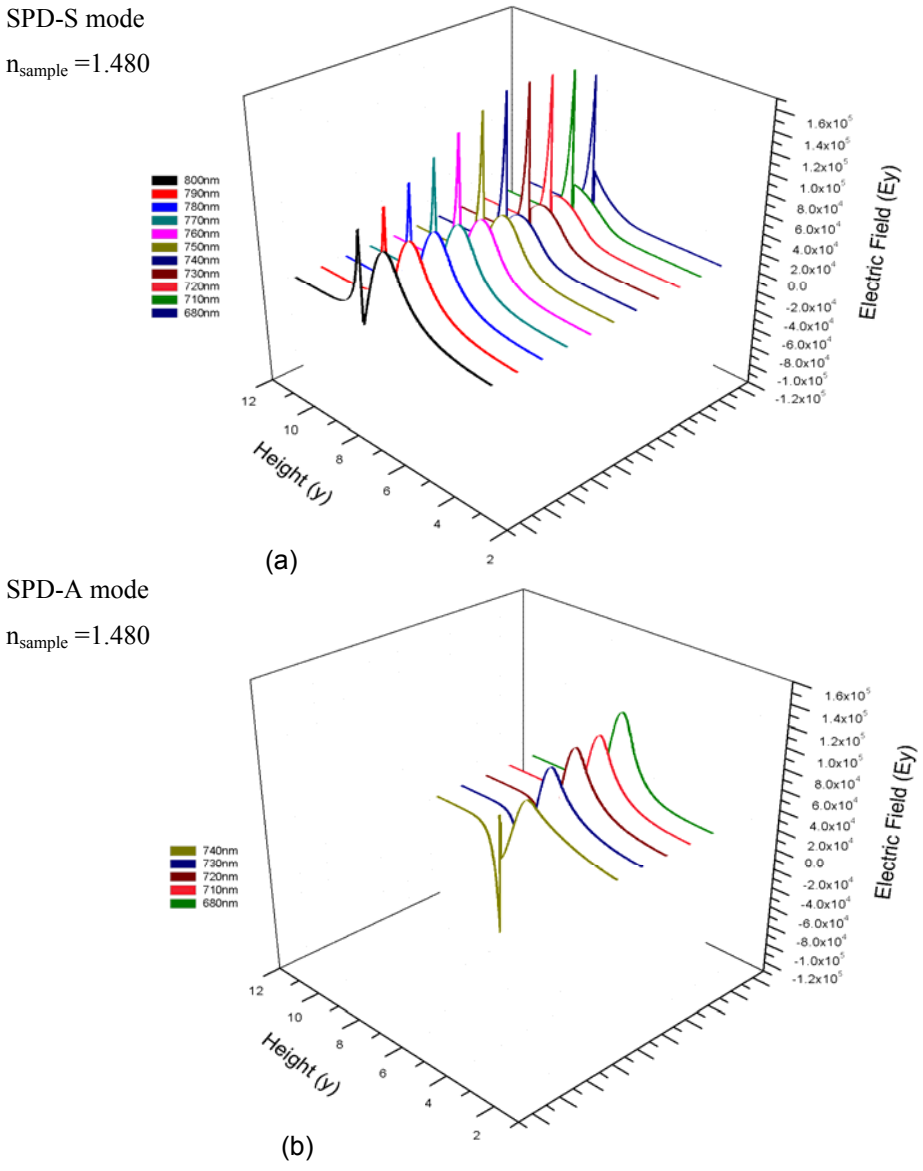

Figure 4-5 Leaky mode filed profile

As Figure 4-5 (a) demonstrates, the field strength of the SPD-S mode in the dielectric waveguide region, grows as the wavelength increases. Conversely, the SPD-A mode's field strength in dielectric waveguide region decreases as the wavelength increases, as shown in Figure 4-5 (b).

4.3 Mode Transmission through the SPR Sensor Head

Mode transmission through the SPR sensor head happens via the conversions of eigen modes at each boundary. Figure 4-6 demonstrates a light transmission process in an integrated optical waveguide type SPR sensor, when the refractive index of an analyte only allows waveguiding of a single mode. In the designed SPR sensor head, the mode conversion happens at the abrupt boundaries, before and after the sensor head.

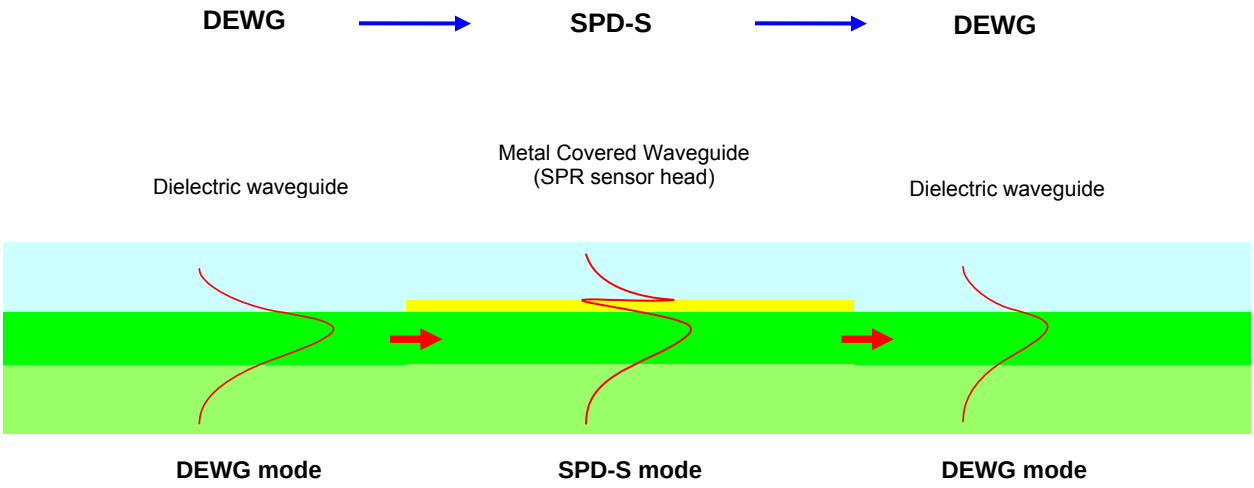

Figure 4-6 Energy transmission process of an integrated optical SPR sensor in a single mode guide condition

When the refractive index of an analyte on the gold layer allows double mode condition, both the SPD-S and SPD-A modes are excited at the input end of the sensor head. The excited SPD-S and SPD-A modes propagate in a SPD-SA hybrid mode form and reconverts into the DEWG mode at the end of the SPR sensor head. Figure 4-7 schematically demonstrates the energy conversion process.

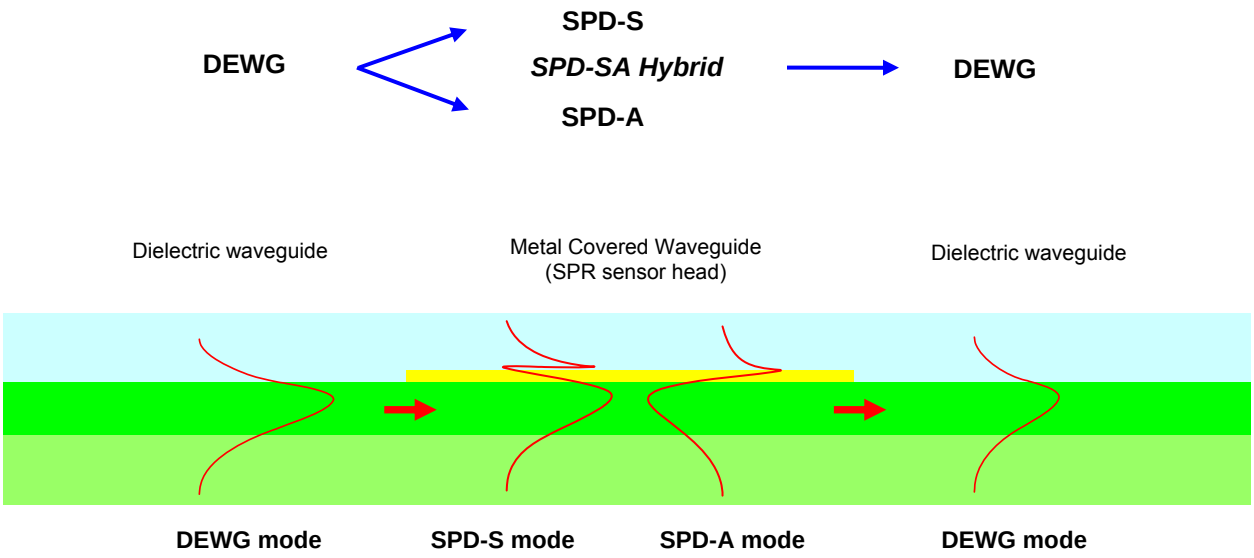

Figure 4-7 Energy transmission process of an integrated optical SPR sensor in a double mode guide condition

4.4 Mode Conversion Efficiency at a Sensor Head Boundary

When a guided optical mode arrives at a boundary and the energy is transferred into a second region, the overlap of the field profiles of the eigen modes in each region governs the conversion efficiency between the modes. Figure 4-8 demonstrates the representative field profiles of the

SPS-S modes at the wavelength of 680 nm and 800 nm and a DEWG mode at the wavelength of 740 nm.

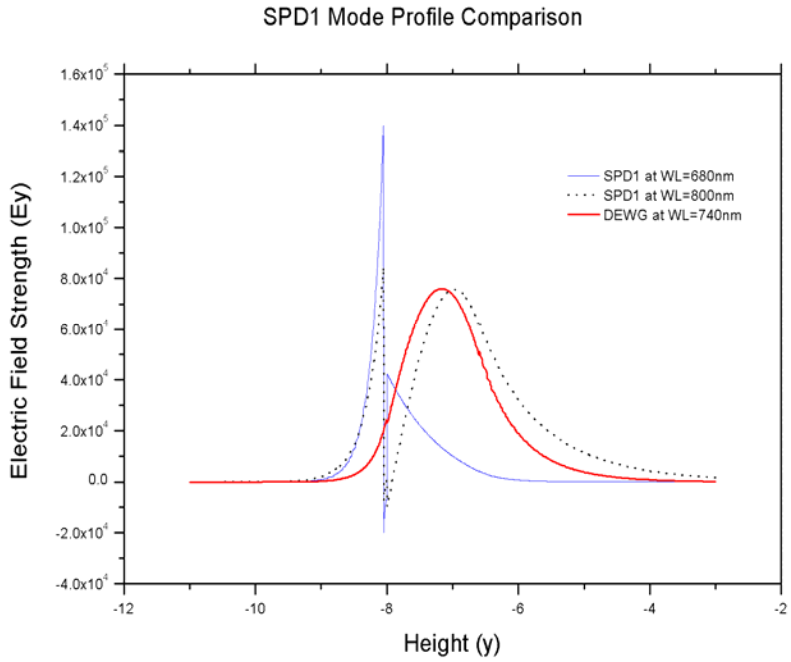

Figure 4-8 Representative field profiles of SPD-S modes and DEWG mode

As the graphs in figure 4-8 shows, at the wave length of 800 nm the SPD-S mode has a field profile that is very similar to that of the DEWG mode.

The field profiles of SPD-A mode are shown in Figure 4-9. The figure demonstrates the field profiles of the SPD-A mode at a wavelength of 680 nm and 750 nm respectively and the field profile of the DEWG mode at a wavelength of 740 nm.

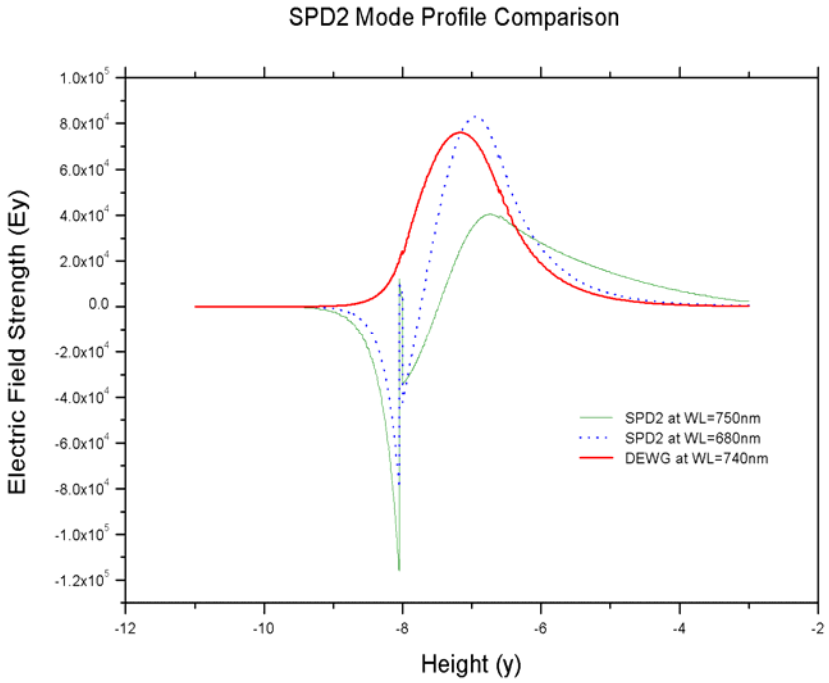

Figure 4-9 Representative field profiles of SPD-A modes and DEWG mode

The efficiencies in the conversion of the energy from the DEWG mode to either or both modes in the metal covered regions were calculated from the overlap integral. Equation 2 shows the power conversion coefficient.

$$a_{v\mu} = 2\int_{-\infty}^{+\infty}\int E_i \times H_{v\mu}^{*} dxdy \qquad (2)$$

4.4.1 Mode conversion at the input boundary of SPR sensor head

At the input boundary, the guided DEWG mode converts to the SPD-S mode or both the SPD-S and the SPD-A modes depending on the refractive index of the analyte on the sensor head.

i) Conversion of the DEWG mode to the SPD-S mode

Figure 4-10 illustrates the overlap integral of the DEWG mode with the SPD-S as representative of the energy conversion between these modes.

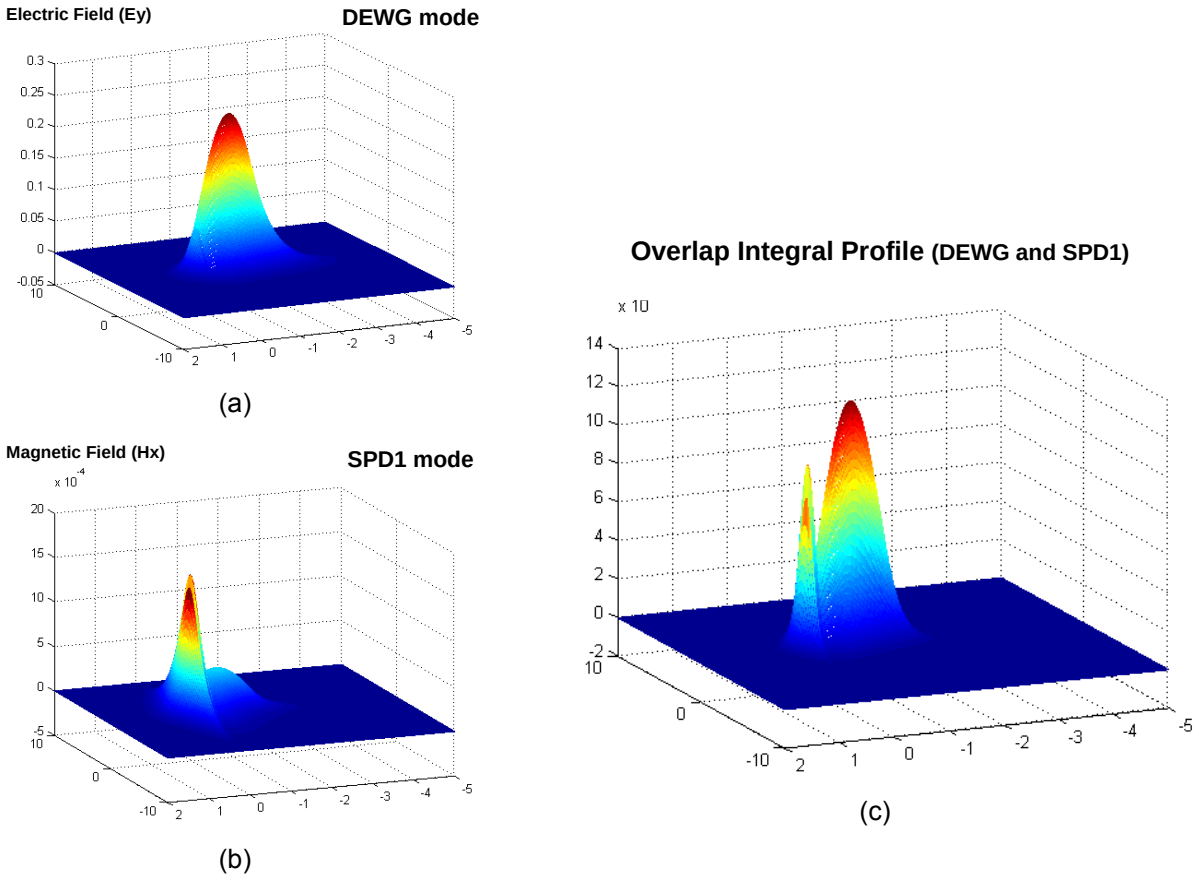

Figure 4-10 Mode conversion from DEWG mode to SPD-S mode

(a) DEWG mode field profile, (b) SPD-S mode field profile, (c) Overlap integral profile of DEWG and SPD-S mode

ii) Conversion of the DEWG mode to the SPD-A mode

Figure 4-11 illustrates the overlap integral of the DEWG mode with the SPD-A mode as representative of the energy conversion between these modes.

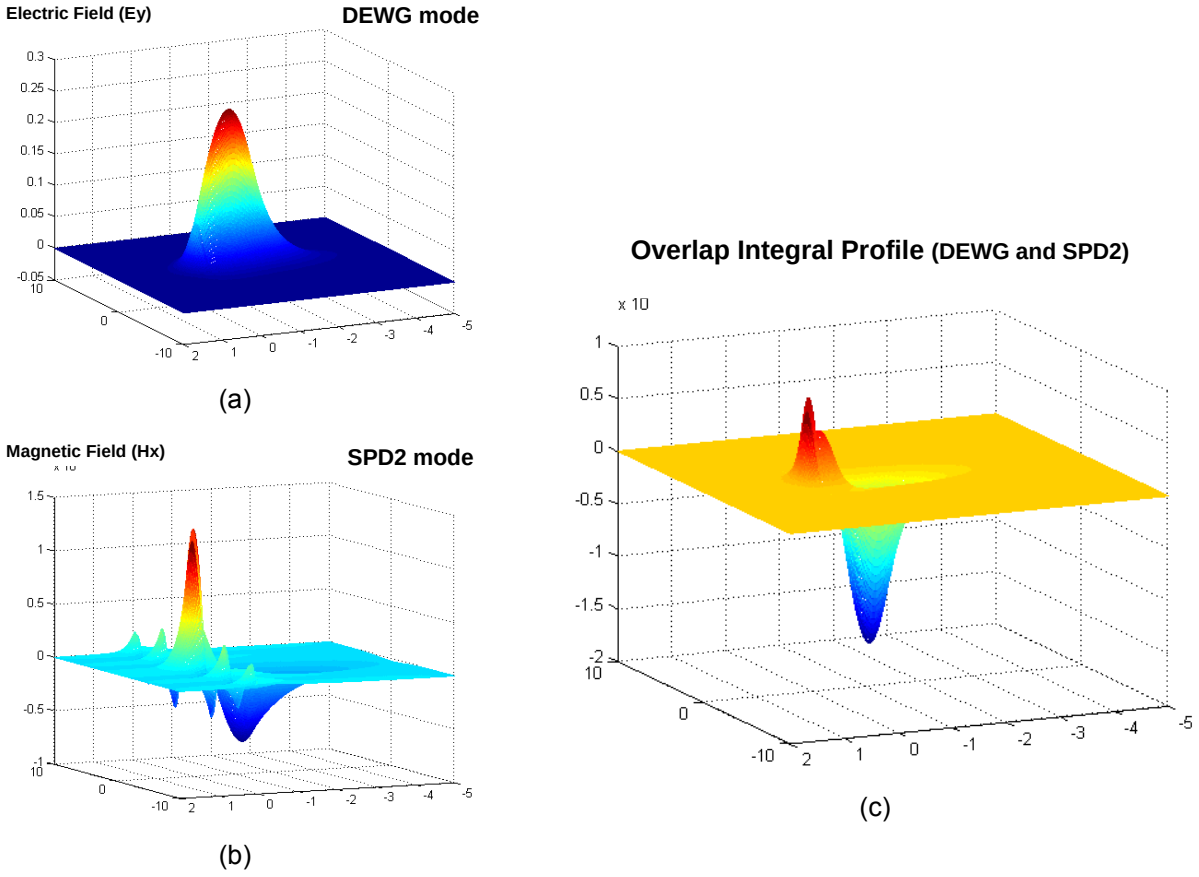

Figure 4-11 Mode conversion from DEWG mode to SPD-A mode

(a) DEWG mode field profile, (b) SPD-A mode field profile, (c) Overlap integral profile of DEWG and SPD-A mode

iii) Refractive index dependence of the mode conversion efficiency

As demonstrated in Figure 4-8 and 4-9, the field profiles of the eigen modes in the SPR sensor head are affected by the refractive index of analyte on top of the sensor. The variation of field profile results in mode conversion efficiencies at the sensor head boundaries. Figure 4-12 shows the refractive index dependence of the mode conversion efficiency.

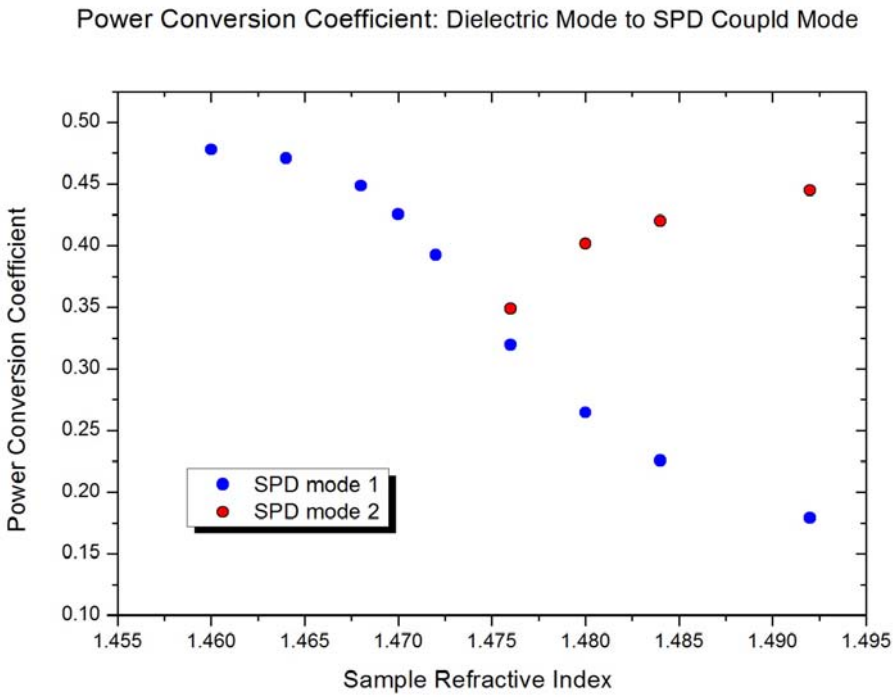

Figure 4-12 Refractive index dependence of mode conversion efficiency

As shown in figure 4-12, conversion efficiency from the DEWG mode to the SPD-S mode decays as the refractive index increases. However at the analyte refractive index of 1.476, the SPD-A mode begins to become an allowed mode and the conversion efficiency into that mode increases as the refractive index increases.

4.4.2 Decay constant of eigen modes in SPR sensor head

Figure 4-13 illustrates the refractive index dependence of the decay constant of the eigen modes. In contrast to the mode conversion efficiency behavior, the decay constant of the SPD-S mode increases as the analyte refractive index increases while the SPD-A mode's decay constant shows opposite behavior.

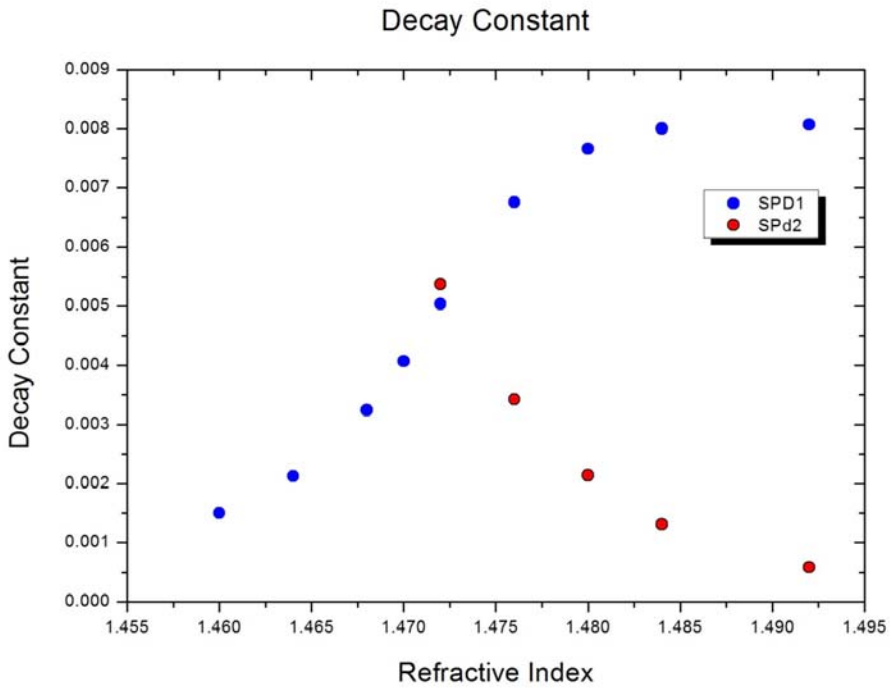

Figure 4-13 Refractive index dependence of eigen modes' decay constant

4.4.3 Excited SPD-SA Hybrid mode

i) Electric field profiles of the SPD-SA hybrid mode

Electric field profiles of the SPD-SA hybrid mode is demonstrated in Figure 4-14. The file profile of SPD-SA hybrid mode is the superposition of the fields of SPD-S and SPD-A modes.

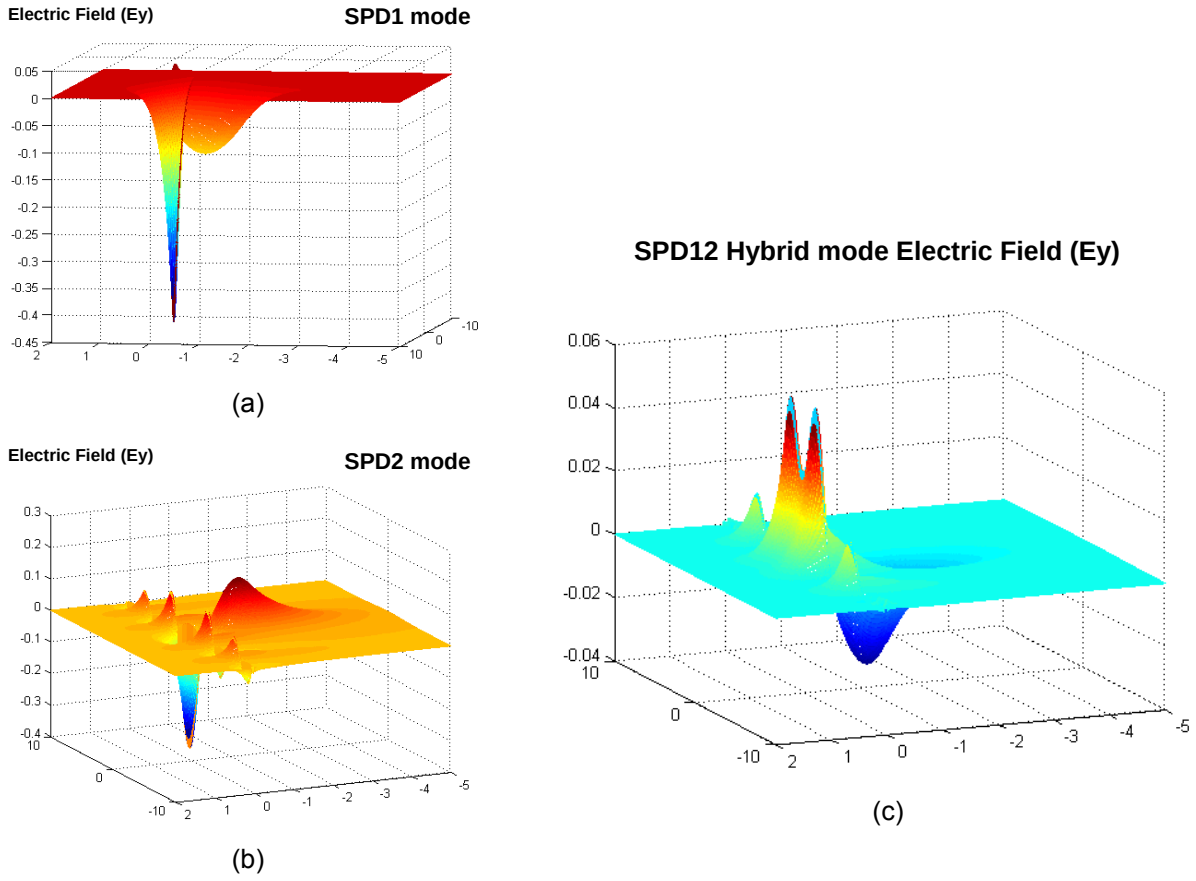

Figure 4-14 Electric field profile of SPD-SA hybrid mode

(a) Electric field profile of SPD-S mode, (b) Electric field profile of SPD-A mode, and (c) Electric field profiles of SPD-SA Hybrid mode

ii) Magnetic field profiles of the SPD-SA hybrid mode

Magnetic field profiles of the SPD-SA hybrid mode was calculated from the superposition of SPD-S and SPD-A mode's magnetic fields and illustrated in Figure 4-15.

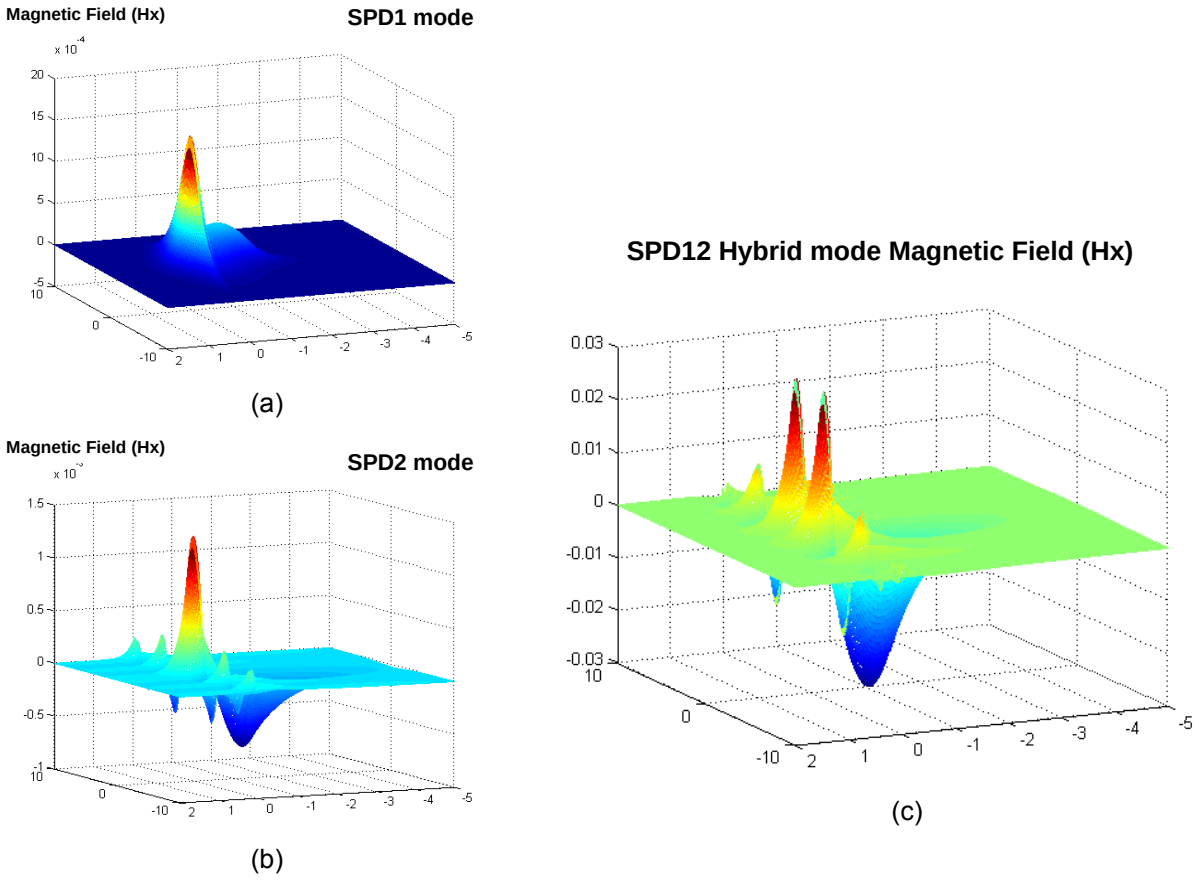

Figure 4-15 Magnetic field profile of SPD-SA hybrid mode

(a) Magnetic field profile of SPD-S mode, (b) Magnetic field profile of SPD-A mode, and (c) Magnetic field profiles of SPD-SA Hybrid mode

4.4.4 Mode conversion at the output boundary of SPR sensor head

In the case of only a single SPD-S mode guided condition, only the SPD-S mode will be converted to the DEWG mode and field conversion efficiency calculation procedure will be similar to the process demonstrated in Figure 4-10. When the SPD-SA hybrid mode exists, the excitation of the DEWG mode will depend on the field profile of SPD-SA hybrid mode. The mode conversion process from the SPD-SA hybrid mode to the DEWG mode is demonstrated in Figure 4-16.

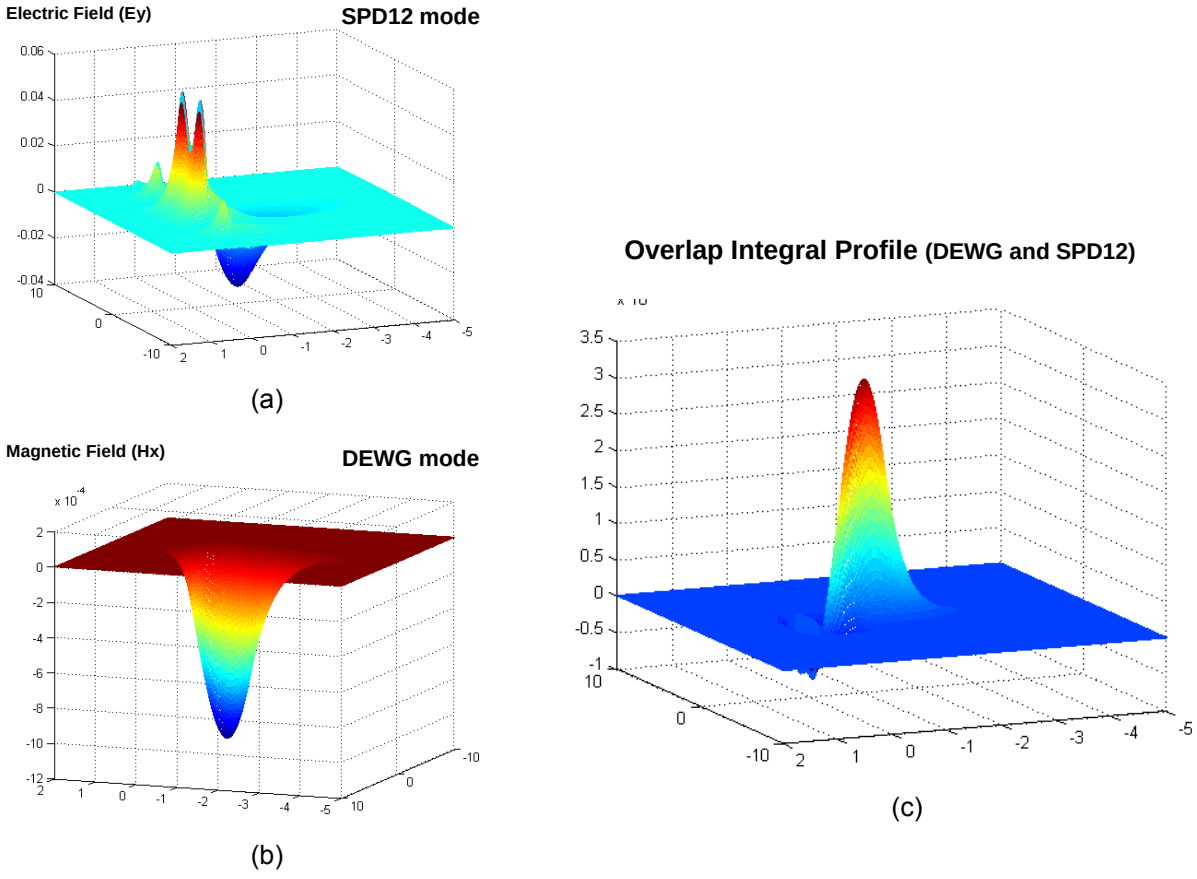

Figure 4-16 Mode conversion from SPD-SA Hybrid mode to DEWG mode

(a) Electric field profile of SPD-SA Hybrid mode, (b) Magnetic field profile of DEWG mode, and (c) Overlap integral profile of SPD-SA Hybrid mode and DEWG mode

4.4.5 Refractive index dependence of transmission

The refractive index dependence of the transmission characteristic is illustrated in Figure 4-17. The calculation was performed for sensor head lengths of 15, 20, 25, 100, and 400 microns respectively. As the figure shows, the shorter the sensor head length, the larger the transmission contrast is.

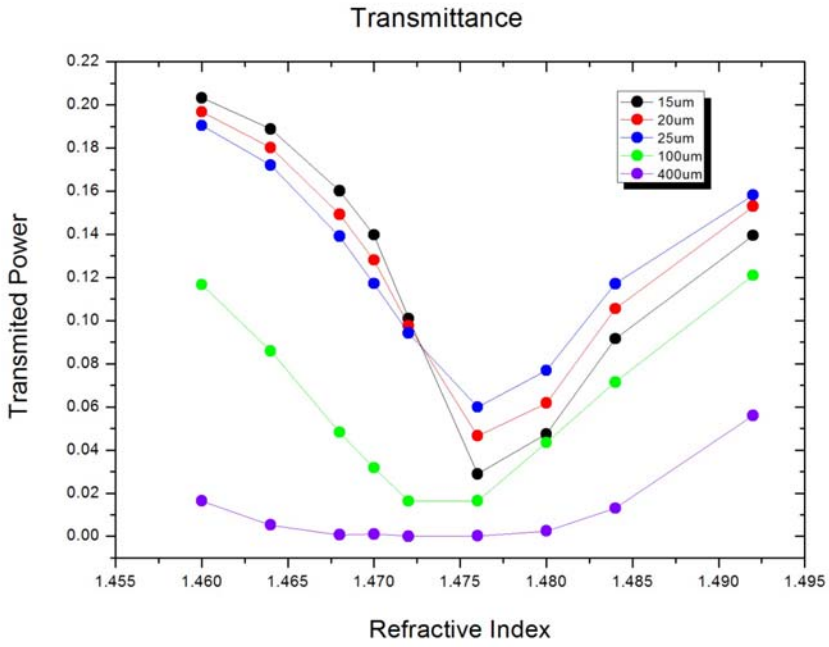

Figure 4-17 Mode transmission: analyte refractive index and sensor head length dependence

When the sensor head length is short, the mode conversion efficiency is the dominant factor for the transmittance spectrum behavior. However, as the senor head become longer, the mode propagation decay constant become significant in making the transmission spectrum.

4.5 Sensitivity

If we use the above device as an intensity modulation type SPR sensor, the refractive index dependence of SPD-S mode can be used as a measure of refractive index variation. In Figure 4-17, if we use the refractive index range 1.470 to 1.472 for calculating sensitivity of the sensor, the sensor sensitivity is calculated as follows.

(20 um sensor head length is supposed)

$$S_{(dB/RIU)} = \frac{1}{\Delta n}\log\left(\frac{P_{Total(n_1)}}{P_{Total(n_1+\Delta n)}}\right)$$

$$= \left|\frac{\log(P_{Total(n_1)}) - \log(P_{Total(n_1+\Delta n)})}{\Delta n}\right|$$

$$= \left|\frac{-1.0089 + 0.8928}{1.472 - 1.470}\right|$$

$$= -\frac{0.1161}{0.002}$$

$$= -58.05 \text{ dB·RIU}^{-1}$$

4.6 Conclusion

In conclusion, a mode conversion type integrated optical SPR sensor has been designed and the characteristics of the transmission spectrum based on mode conversion efficiency and mode propagation have been studied. Compared with conventional absorption type or interferometer type sensors, the newly developed mode conversion type SPR sensor has a significantly reduced sensor head size and is a relatively simple structure. The aforementioned characteristics of the

mode conversion type sensor will provide great advantages in realizing true Lab-on-a-Chip sensor system.

CHAPTER 5 DEVICE DESIGN

The proposed integrated optical SPR sensor based on optoelectronic platform is composed of a dielectric waveguide based sensor head and an integrated photodetector. Fig. 5-1 shows the schematic view of the entire SPR sensor.

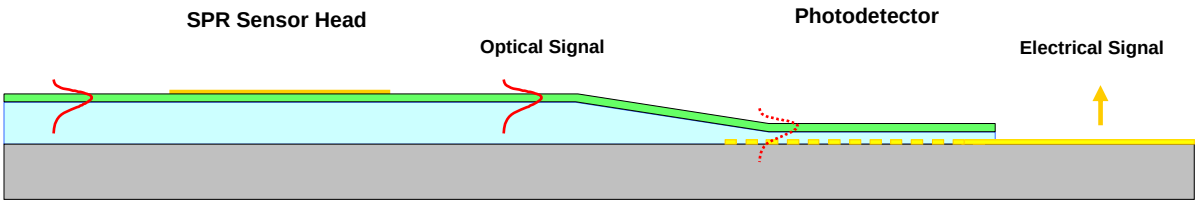

Figure 5-1 Schematic view of the cross-section of the designed SPR sensor

As described earlier, in a dielectric waveguide based SPR sensor, a guided mode excites the surface plasmons on the gold layer [16]. Therefore, guided mode control is essential in achieving highest sensitivity from the sensor head. Fig. 5-2 shows schematic views of the waveguide mode and the surface plasmon mode.

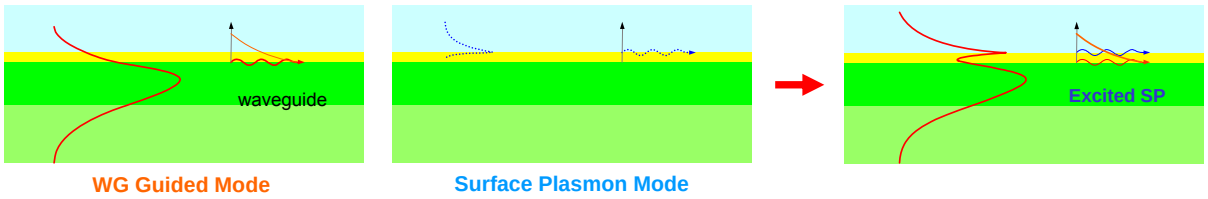

Figure 5-2 Surface plasmon excitation with waveguide mode

The inverted rib type waveguide has been selected for the developed SPR sensor head because it presents a flat top surface on which to attach the micro-fluidic channel components. Fig. 5-3

shows a cross section of inverted rib type waveguide. From the waveguide material characterization, the refractive indices of 1.60 and 1.58 are selected for the guiding and cladding materials respectively. For the simulation of a SPR sensor head, a simple dielectric waveguide without gold layer was modeled as an approximation.

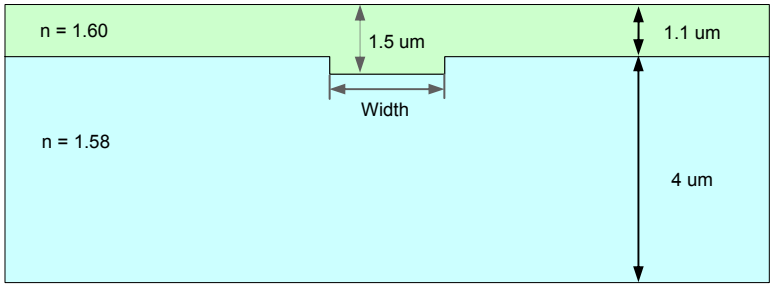

Figure 5-3 Inverted rib type dielectric waveguide for SPR sensor head

While taking into account photolithography based device fabrication tolerance, the waveguide widths on the mask are designed so that the fabricated device maintains a single mode condition in entire scanned wavelength range (λ = 700 ~ 760 nm). From the simulation result, the target dimension of a waveguide is decided as follows. Fig. 5-4 shows field strength distribution around the waveguide.

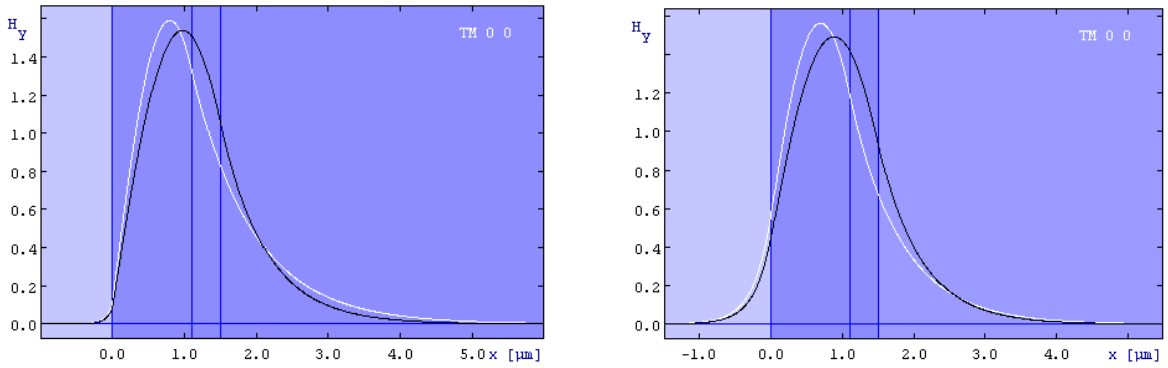

Air cladding (n = 1) Liquid cladding (n = 1.52)

Figure 5-4 Guided mode profile in air and liquid cladding condition

CHAPTER 6 MATERIAL CHARACTERIZTION

The surface plasmon on the gold layer is excited by the mode guided in a dielectric waveguide and the characteristics of the guided mode directly affects to SPR signal. The geometrical dimension and refractive indices of the guiding and cladding layers define the characteristics of the wavevector of the guided modes. Therefore, accurate information on the listed parameters is essential for designing the sensor heads and estimating the expected resonance wavelength. The waveguide for SPR sensor head is made of SU-8 polymer [25] for the guiding layer and siliconoxynitride for the cladding layer. The refractive indices and surface morphologies of the films were carefully studied before fabrication of the actual device.

6.1 m-line Method for Refractive Index Measurement

One of the most commonly used method for measuring the refractive index of a film is the "m-line" method. The refractive indices of SU-8 and siliconoxynitride films have been measured using m-line method [26, 27] in this work.

Fig. 6-1 shows a configuration for m-line method of measuring the refractive index of thin films. A target film is deposited on a substrate with lower refractive index to form a slab waveguide. A prism with higher refractive index is placed on the target film to couple a laser beam into the waveguide.

In the experiment, a beam of laser light was directed into the prism and the incident angle for launching the guided mode was measured by scanning the incident angle. Since the refractive indices of the prism and substrate are known, the refractive index of the target film can be

calculated. In our experiment, a Rutile prism was used for launching the laser beam into the guiding film that was deposited and a commercial microscope glass cover slide was used as the substrate.

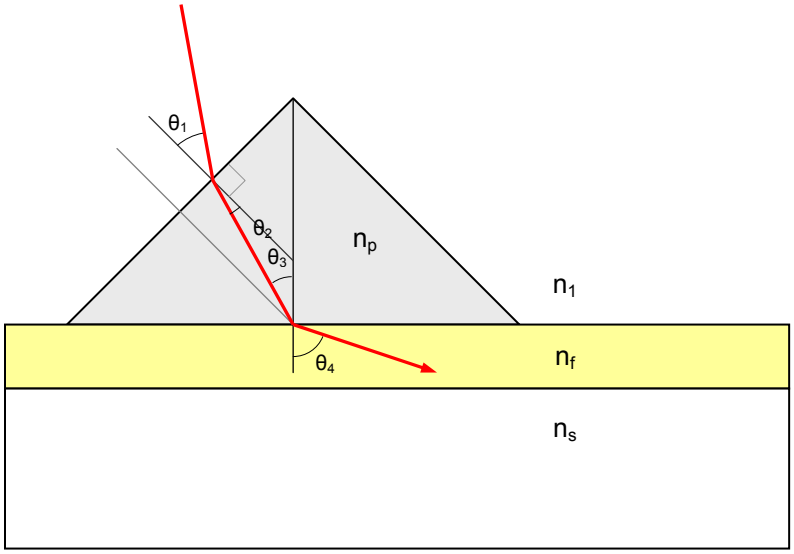

$$n_1 \cdot \sin\theta_1 = n_p \cdot \sin\theta_2$$

$$\theta_2 + \theta_3 = \frac{\pi}{4}$$

$$n_p \cdot \sin\theta_3 = n_f \cdot \sin\theta_4 = n_e$$

Figure 6-1 m-line method based refractive index measurement configuration

Refractive index information of a Rutile prism and a BK-7 cover glass are as follows.

• Refractive indices of Rutile coupling prism depending on the wavelengths

Optics For Research, Inc. (http://www.ofr.com/oc-30_prism.htm)

For the experiment, the refractive indices of the materials were deduced at the wavelength of 700 nm.

• Rutile prism's Refractive index at $\lambda = 0.700$ μm $n_p = 2.548$

• Glass substrate's Refractive index at $\lambda = 0.700$ μm $n_s = 1.520$

The equations used for the refractive index calculation were as follows.

$$\theta_3 = \frac{\pi}{4} - \theta_2$$

$$n_p \cdot \sin\theta_2 = n_1 \cdot \sin\theta_1$$

$$\sin\theta_2 = \frac{n_1}{n_p} \cdot \sin\theta_1 \qquad (n_1 = 1)$$

$$\theta_2 = \sin^{-1}\left(\frac{\sin\theta_1}{n_p}\right)$$

- $n_e = n_p \cdot \sin\theta_3$

$$= n_p \cdot \sin\left(\frac{\pi}{4} - \theta_2\right)$$

$$= n_p \cdot \sin\left\{\frac{\pi}{4} - \sin^{-1}\left(\frac{\sin\theta_1}{n_p}\right)\right\}$$

- $$m\pi = k_o \cdot t_g \cdot \sqrt{n_g^{\,2} - n_e^{\,2}} - a\tan\left(\frac{n_g^{\,2}}{n_c^{\,2}} \cdot \sqrt{\frac{n_e^{\,2} - n_c^{\,2}}{n_g^{\,2} - n_e^{\,2}}}\right) - a\tan\left(\frac{n_g^{\,2}}{n_s^{\,2}} \cdot \sqrt{\frac{n_e^{\,2} - n_s^{\,2}}{n_g^{\,2} - n_e^{\,2}}}\right)$$

$$\frac{2\pi}{\lambda} \cdot t_g \cdot \sqrt{n_f^{\,2} - n_e^{\,2}} - a\tan\left(n_f^{\,2} \cdot \sqrt{\frac{n_e^{\,2} - 1}{n_f^{\,2} - n_e^{\,2}}}\right) - a\tan\left(\frac{n_f^{\,2}}{n_s^{\,2}} \cdot \sqrt{\frac{n_e^{\,2} - n_s^{\,2}}{n_f^{\,2} - n_e^{\,2}}}\right) = m \cdot \pi$$

6.2 Refractive Index of Siliconoxynitride and SU-8 Films

The elemental constituents of siliconoxynitride are silicon, oxygen and nitrogen. The optical and chemical properties of siliconoxynitride can be controlled by managing the ratio of oxygen and

nitrogen concentration in the film. In this research, the siliconoxynitride layer was grown using a plasma enhanced chemical vapor deposition (PECVD) method [28-31].

In the deposition process, four gases were flown into the deposition chamber; silane, nitrous oxide, ammonia, and nitrogen. Silane gas provides the elemental silicon to the composition of the grown material. Nitrous oxide and ammonia provide oxygen and nitrogen to the film respectively. Nitrogen gas is for balancing the pressure inside the chamber and also for lowering the temperature of the gas mixture.

The characterization process was performed by regulating the temperature and gas flow ratio of nitrous oxide and ammonia inside of the chamber. Table 6-1 illustrates the refractive indices of the films depending on the deposition condition.

Table 6-1 Refractive indices of silicon-oxynitride films depending deposition condition

Film ID	**Refractive Index** (from m=0 mode)	**Film Deposition Recipe**							
		Ratio (NH_3 :NO_2)	**NH_3**	**NO_2**	**SiH_4**	**N_2**	Power (W)	DC (V)	Temp (°C)
H2-low	1.649	1 : 3	**6**	**18**	200	600	100	8	250
H3-low	1.631	1 : 3.5	**6**	**21**	200	600	100	8	250
H1-low	1.619	1 : 4	**5**	**20**	200	600	100	8	250
H4-low	1.582	1 : 6	**6**	**36**	200	600	100	8	250
H5-high	1.570	1 : 6	**6**	**36**	200	600	150	8	300
H8-high-80	1.570	1 : 8	**4**	**32**	200	600	150	8	300
H8-high-60	1.569	1 : 8	**4**	**32**	200	600	150	8	300
H8-low-60	1.580	1 : 8	**4**	**32**	200	600	100	8	250
H9-high	N/D	1 : 8	4.5	36	200	600	150	8	300
H7-high	N/D	1 : 9	4	36	200	600	150	8	300
H6-high	N/D	1 : 18	2	36	200	600	150	8	300

Also from the m-line measurement, the refractive index of SU-8 film was determined to be 1.60. For the actual device fabrication, a siliconoxynitride film with the refractive index of 1.580 was selected for the cladding layer of the waveguide.

6.3 Observation of film surface morphologies

The surface roughness of the guiding layer and the gold sensor film is expected to adversely affect to resonance in the SPR spectrum. Therefore, the surface morphologies of an SU-8 film and a gold layer for the sensor head have been measured using an atomic force microscope (AFM). Fig 6-2 (a) and (b) show the surface morphology images captured by AFM.

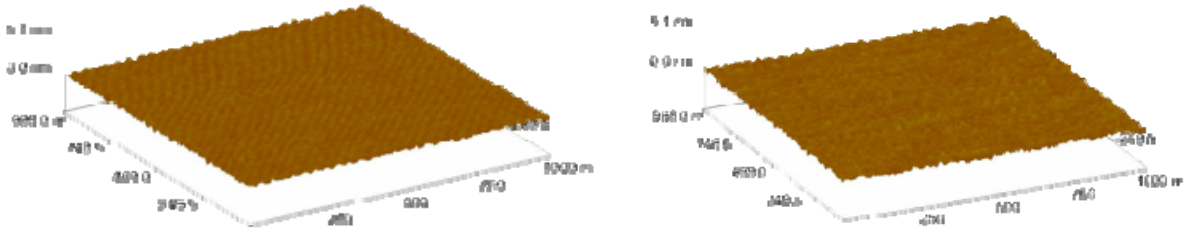

(a) (b)

Figure 6-2 Atomic force microscope images:
(a) Surface of SU-8 guiding layer and (b) Surface of gold sensor head layer

CHAPTER 7 DEVICE FABRICATION

Micro SPR sensors based on optoelectronic platform have been designed and fabricated on a GaAs substrate. On a single completed SPR sensor chip, 54 individual sensor units were fabricated. A SPR sensor unit is composed of two sections: a waveguide based sensor head and an integrated photodetector.

7.1 SPR Sensor Composition

7.1.1 SU-8 Guiding Layer and Sensor Head

The sample with a patterned silicon-oxynitride film was spin coated with SU-8 polymer. The SU-8 film was removed in the regions of the MSM electrode contact pads to allow access for electrical probes. The grooves filled with the SU-8 polymer formed the light guiding channel. The thickness of the film was 1.2 μm outside of the grooves. Finally the SPR sensor head was formed by depositing 5-nm-thick chromium and 45-nm-thick gold layers in the middle region of the waveguides using photolithography and lift off process. Each waveguide was covered with different lengths of the gold sensing layer in order to experimentally determine the optimum sensor head length. Figure 7-1 shows a scanning electron microscope picture of a groove that will be filled with SU-8 for the inverted rib waveguide.

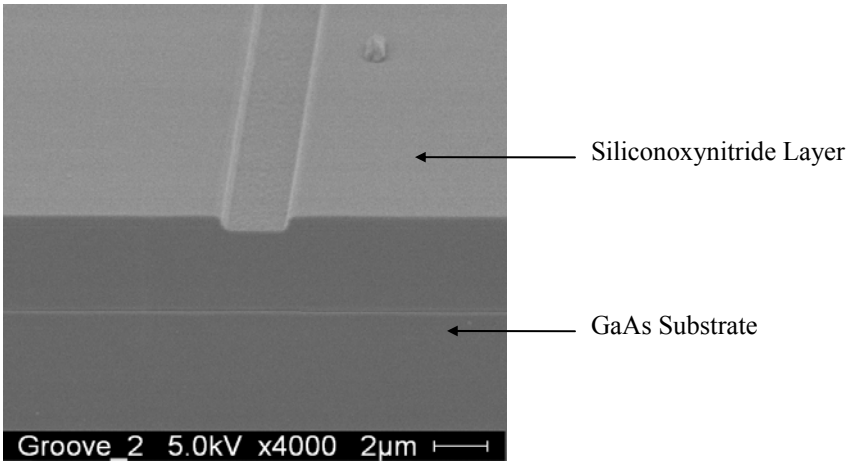

Figure 7-1 A groove made on siliconoxynitride layer for inversed rib type waveguide

7.1.2 Siliconoxynitride Buffer Layer

After the photodetector fabrication process, another layer of 4 μm thick silicon-oxynitride was deposited and patterned. This silicon-oxynitride layer functions as a cladding layer of the optical waveguides that spans from the input end of the device to the individual MSM photodetectors [32-34]. The patterning of the silicon-oxynitride layer is composed of three steps. The first patterning step is to reduce the thickness of the cladding layer on top of the interdigitated electrodes of the MSM photodetector. The cladding layer on top of the interdigitated electrodes region is thinned down to 1μm so as to provide reasonable coupling of the energy in the guided mode into the photo-sensitive substrate and without suffering significant scattering of the light due to the abrupt discontinuity. The layer also serves as an electrical insulator by separating the SU-8 guiding layer from the interdigitated electrodes. When the SU-8 based guiding layer was allowed to touch the MSM electrodes, electrical breakdown can occur in the SU-8 and leakage current can flow when bias voltage is applied between electrodes. This shaping of the cladding layer was performed with a RIE (Reactive Ion Etching) process to give a gentle slope to the

thickness transition region (Figure 7-2). The second patterning step of the cladding layer is the opening of the electrode contact pad windows. The final patterning step delineates a groove for the inverted rib waveguide. The grooves that are 300nm deep by 2.5 μm wide, and extend from the input end of the device to the individual MSM interdigitated electrodes.

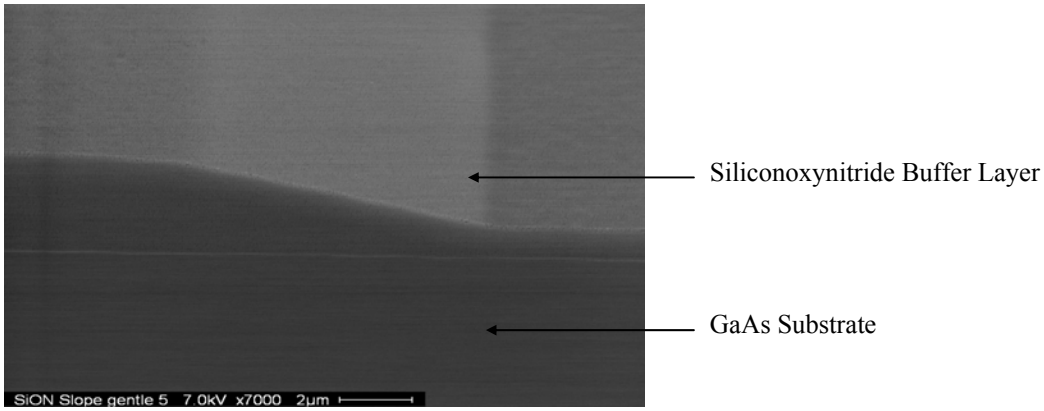

Figure 7-2 RIE etched gentle slope of siliconoxynitride buffer layer

7.1.3 MSM Photodetector

The device fabrication process started with the fabrication of the MSM photodetectors [35, 36]. A 200nm thick silicon-oxynitride layer was deposited by PECVD and patterned using photolithography and reactive ion etching to leave narrow strip windows. This insulation layer serves to minimize any leakage current from the electrodes and contact pads and hence to reduce noise due to dark current [37, 38]. On the insulation layer, 5 nm of chromium and 250 nm of gold layers were deposited and patterned through the lift-off process. The width of the interdigitated electrodes was 2.5 μm and the gap between them was also 2.5 μm. Only the sections of the interdigitated electrodes that cross with the waveguide are actually in contact with

the GaAs substrate through a window opened in the siliconoxynitride film. Figure 7-3 and 7-4 show optical microscope images of the interdigitated electrodes.

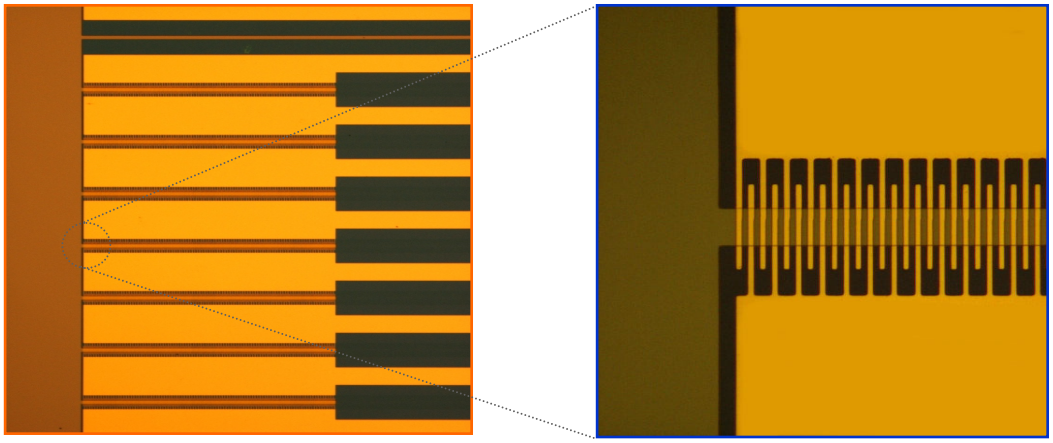

(a) (b)

Figure 7-3 Optical microscope images of (a) Array of MSM photodetectors (b) Magnified image of unit MSM photodetector's interdigitated electrodes

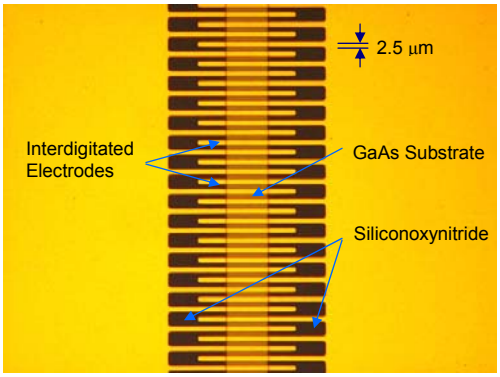

Figure 7-4 Dimensions of MSM photodetector interdigitated electrodes

7.2 Fabrication Steps

The fabrication process of the optoelectronic platform based integrated optical SPR sensor starts with the fabrication of a MSM photodetector array followed by an array of integrated optical SPR sensor heads fabrication. The fabrication process for SPR sensor system is composed of eight photolithography steps, three steps are for MSM photodetectors fabrication and the rest of the five steps are for the fabrication of integrated optical SPR sensor heads. The fabrication steps are described as follows.

i) Siliconoxynitride Layer Deposition on a GaAs substrate

The first fabrication step of the optoelectronic platform based integrated optical SPR device was the deposition of a siliconoxynitride layer on a GaAs substrate with a PECVD (Plasma Enhanced Chemical Vapor Deposition) machine, which was also the first fabrication step of MSM photodetectors. Table 7-1 shows a siliconoxynitride deposition condition with a PECVD machine.

Table 7-1 Siliconoxynitride layer deposition condition

Recipe ID	Deposition Condition						
SION_H8_LOW	NH3 (sccm)	NO2 (sccm)	SiH4 (sccm)	N2 (sccm)	Power (W)	DC (V)	Temp (°C)
	4	32	200	600	100	8	250

Figure 7-5 shows the schematic view of a siliconoxynitride layer covered GaAs substrate. The deposition time was 10 minutes and the grown siliconoxynitride film thickness was 400 nm.

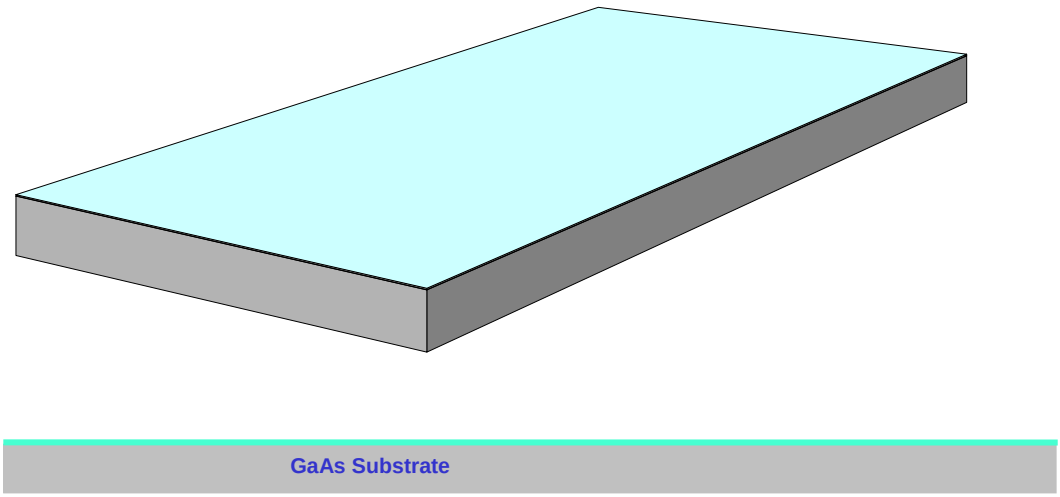

Figure 7-5 Siliconoxynitride layer deposition on a GaAs substrate

ii) Siliconoxynitride Insulation Layer Patterning

The deposited siliconoxynitride layer was patterned with a wet etching process using a buffered oxide etchant (BOE). Shipley 1813 photoresist was used as an etching mask and the etching time was 1 minute and 45 seconds. The patterned structure works as an insulation structure of the MSM photodetector to suppress dark current. Figure 7-6 shows the schematic view of the patterned siliconoxynitride layer.

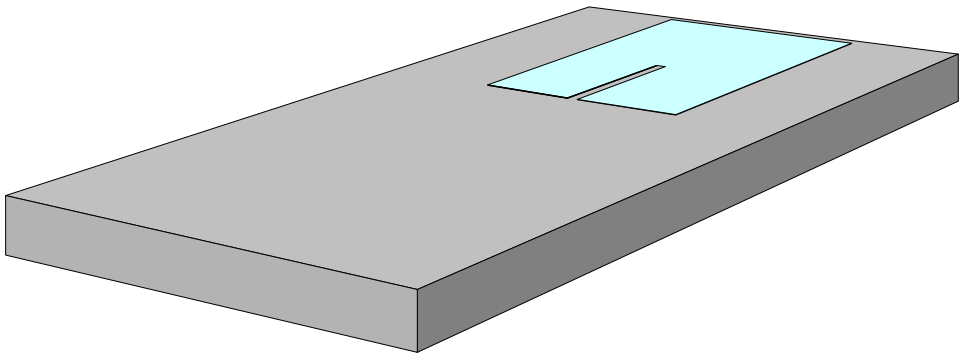

Figure 7-6 Siliconoxynitride structure patterned with BOE etching process

iii) MSM photodetector electrodes patterning

The electrodes for MSM photodetectors were made using a lift off process. NR7-1000PY photoresist was patterned on the substrate and 10 nm of titanium and 250 nm of gold was deposited. The patterned photoresis was removed using a RR2 resist remover after the metal deposition leaving patterned electrodes for MSM photodetectors. Figure 7-7 shows the schematic view of the patterned MSM electrodes.

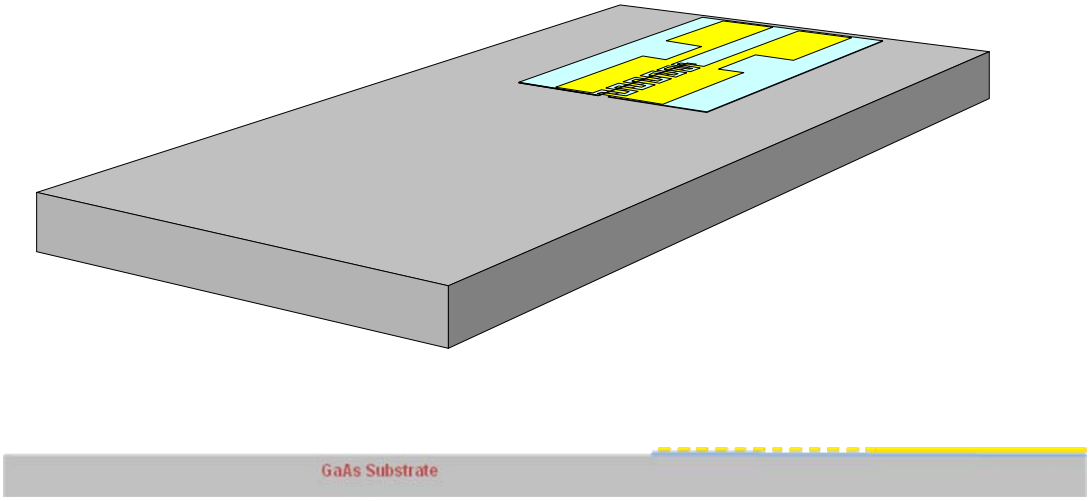

Figure 7-7 Patterned electrodes for a MSM photodetector

iv) Siliconoxynitride deposition for waveguide cladding layer

Another layer of siliconoxynitride was deposited on the pre-made structure using a PECVD machine to structure dielectric waveguide's cladding layer. Table 7-2 shows the deposition condition of the process. The deposition time was 1 hour and 40 minutes and the thickness was 4 microns. Figure 7-8 shows the schematic view of the siliconoxynitride layer deposited substrate.

Table 7-2 Siliconoxynitride layer deposition condition

Recipe ID	Deposition Condition						
SION_H8_LOW	NH3 (sccm)	NO2 (sccm)	SiH4 (sccm)	N2 (sccm)	Power (W)	DC (V)	Temp (°C)
	4	32	200	600	100	8	250

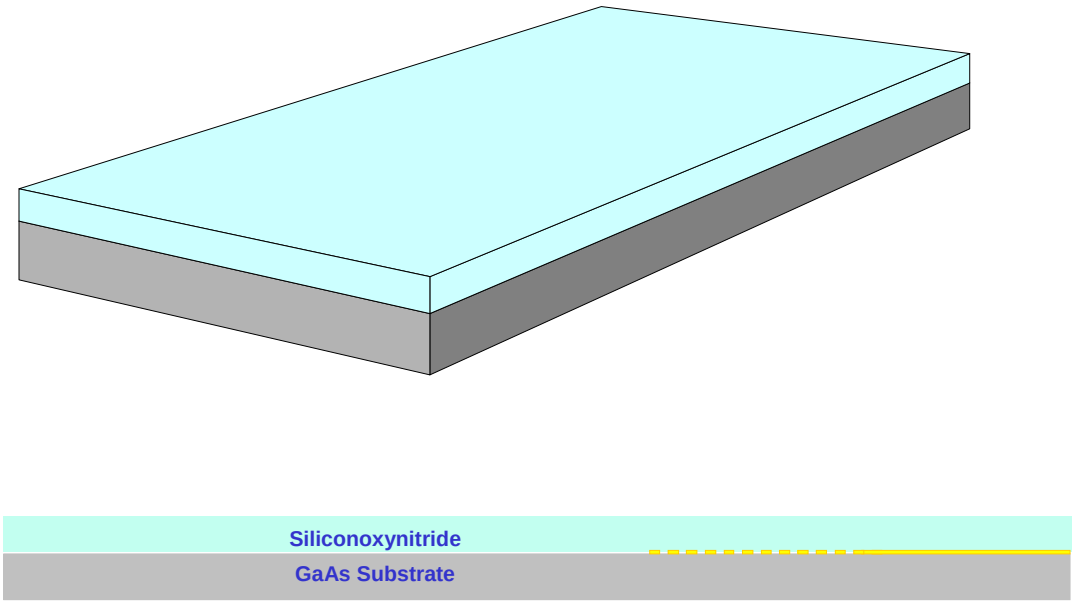

Figure 7-8 Siliconoxynitride layer deposition on the substrate

v) Siliconoxynitride buffer layer slope patterning

In order to couple a guided mode to on-substrate integrated MSM photodetector with minimized light scattering, a gentle slope on the siliconoxynitride layer was made. The thickness of siliconoxynitride clad layer in the sensor head region was 4 microns and the thickness on the

MSM photodetector was reduced down to 1 micron. The fabrication process for the gentle slope is demonstrated in Appendix A.

Table 7-3 Siliconoxynitride layer etching condition

Recipe ID	Etching Condition					
etc_sio5	CF4 (sccm)	O2 (sccm)	Pressure (mTorr)	Power (W)	DC (V)	Temp (°C)
	45	5	75	175	300	25

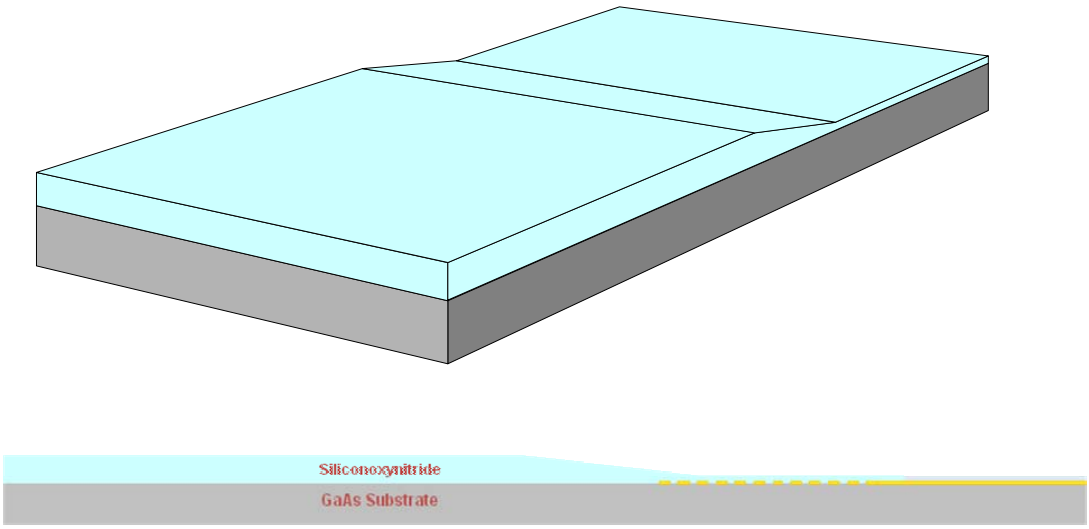

Figure 7-9 Gentle slope given to the siliconoxynitride cladding layer

vi) MSM photodetector electrode contact pad opening

The contact pads of the MSM electrodes were opened by etching the sliconoxynitride layer on the contact pads to read the signal from the integrated photodetectors. The layer was etched with a BOE wet etching process. NR7-1000PY photoresist was used as an etching mask and the

etching time was 5 minutes. Figure 7-10 illustrates the schematic view of the contact pad exposed structure.

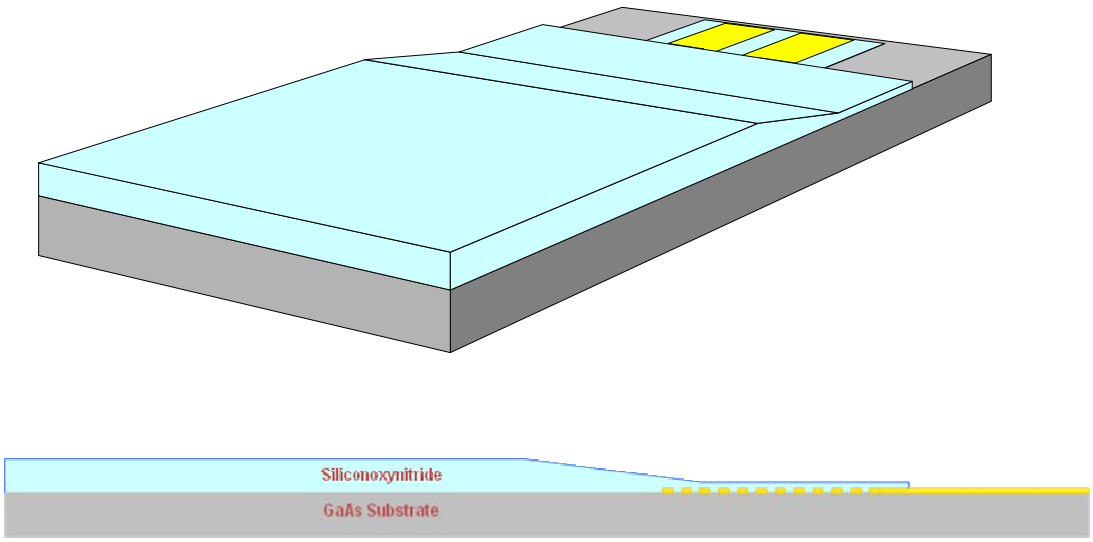

Figure 7-10 Schematic view of the contact pad opened structure

vii) Groove for inverted rib waveguide patterning

Following the contact pad opening, a groove with 2-um-width and 300-nm-depth was made with a RIE etching process. Table 7-4 shows the reactive ion etching condition and the etching time was 6 minutes. Figure 7-11 illustrates the schematic view of the groove patterned cladding structure.

Table 7-4 Siliconoxynitride layer etching condition

Recipe ID	Etching Condition					
etc_sio5	CF4 (sccm)	O2 (sccm)	Pressure (mTorr)	Power (W)	DC (V)	Temp (°C)
	45	5	75	175	300	25

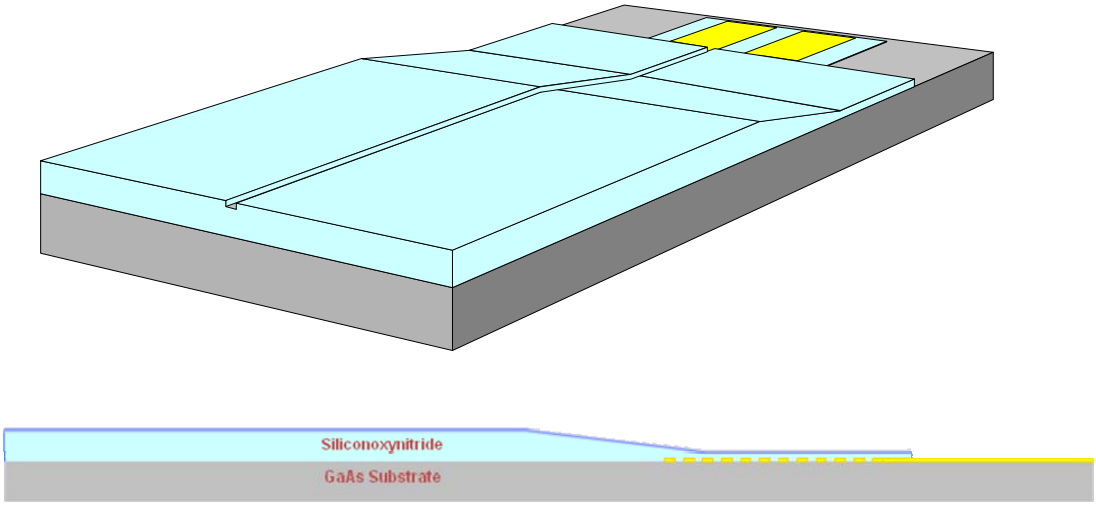

Figure 7-11 Schematic view of the reactive ion etched groove on the siliconoxynitride layer

viii) SU-8 guiding layer coating and patterning

SU-8 polymer was spin coated and patterned with a photolithography process. The groove filled with SU-8 polymer formed inverted rib type optical waveguide. The thickness of SU-8 polymer at the side of the inverted rib structure was 1.2 microns. Figure 7-12 illustrates the schematic view of SU-8 covered structure.

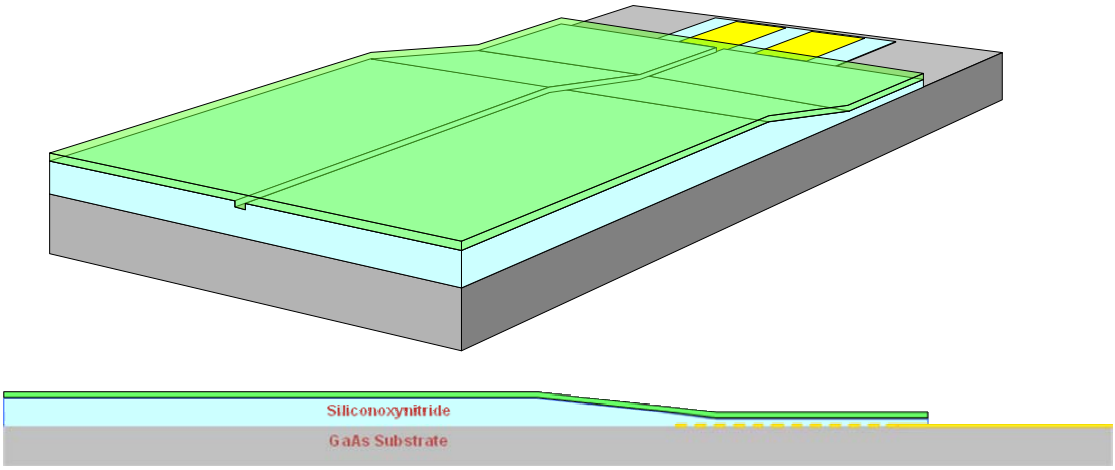

Figure 7-12 SU-8 covering the groove on the siliconoxynitride layer to from a inverted rib waveguide

ix) Gold layer patterning to form a SPR sensor head

As the final step of the fabrication, a thin metal layer was patterned on the inverted rib type dielectric waveguide. 5-nm-titanium and 45-nm-thick gold was deposited and patterned via lift off process using NR7-1000PY photoresist. Figure 7-13 shows the schematic view of the fabricated unit SPR sensor.

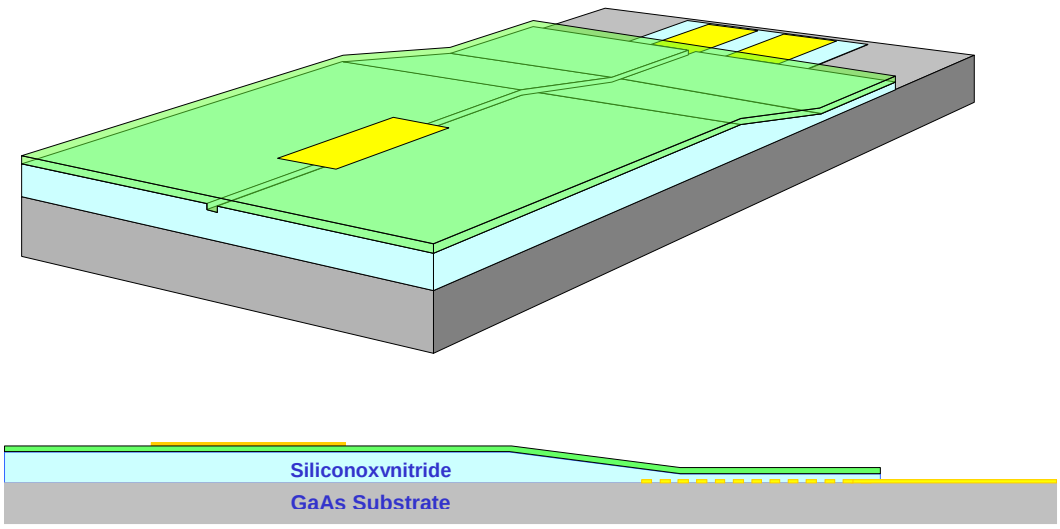

Figure 7-13 The schematic view of the fabricated unit SPR sensor

Figure 7-14 displays a fabricated device array after the fabrication procedure. Figure (a) and (b) show the device before and after the cleaving, which makes end facet for light launcing. 108 unit devices have been fabricated on a 2 x 2cm^2 sized GaAs substrate.

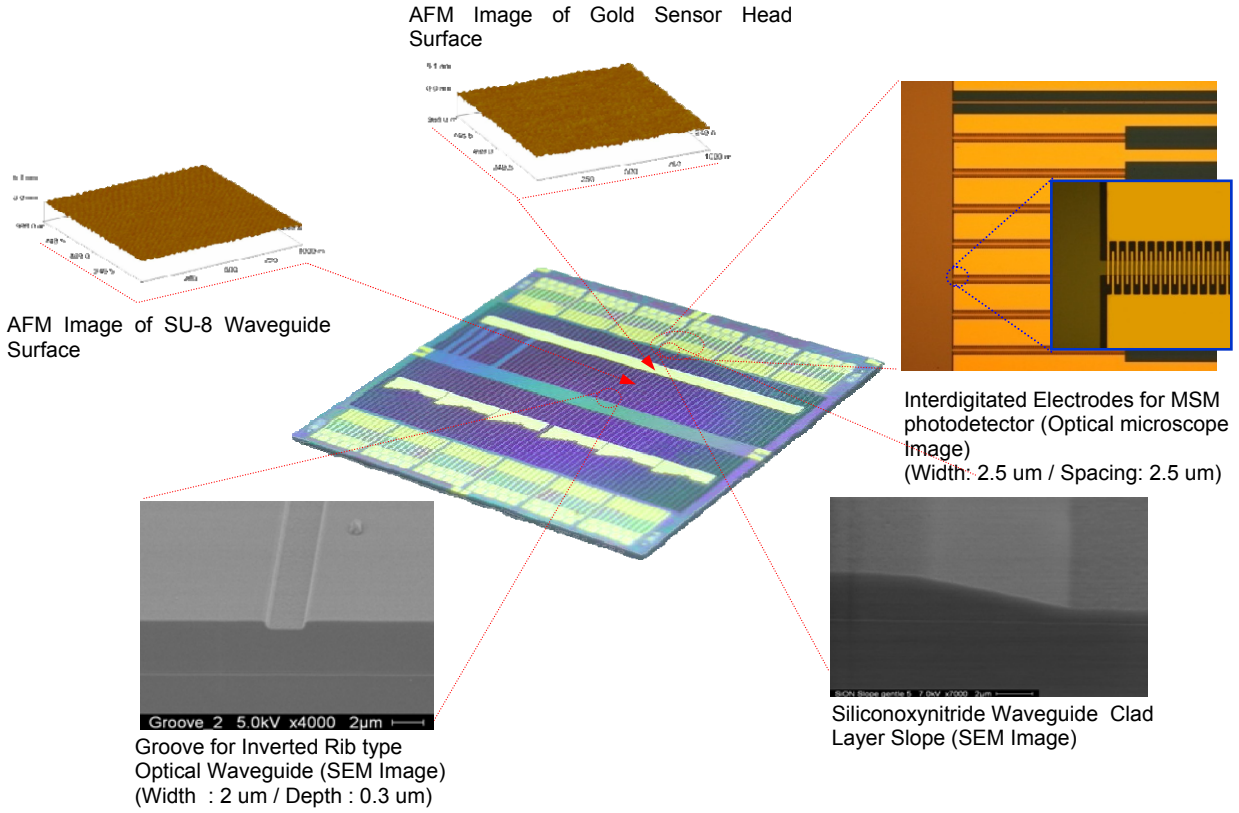

(a)

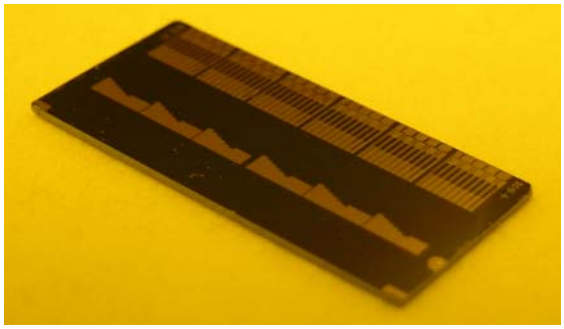

(b)

Figure 7-14 Fabricated SPR device; (a) Device before cleaving and (b) after cleaving

7.3 Fluidic System for Sample Delivery

The next phase is incorporating the fluidic system. The current fluidic system was designed to deliver six samples to six groups of sensor heads. For the completion of fluidic system, PDMS based microfluidic channel – SPR device – fluidics interfacing block bonding and packaging step is required.

7.3.1 Microfluidic Channel

The microfluidic channel was made of PDMS by incorporating a fluidic channel pattern on the layer during the curing process. The first fabrication step is making a mold for the fluidic channel by photolithographically patterning SU-8 on a silicon substrate. The SU-8 pattern had the thickness of 15 μm and was composed of six units. The next step was curing the PDMS elastomer base mixed with the curing agent to a ratio of 10:1. The temperature was ramped up at a rate of 10 ºC/hr until it reached 90 ºC and cured until completely hard. The total curing time was 12 hours including the temperature ramping period [25].

7.3.2 Micro to Macro Fluidic Interconnection

Although the device is of micrometer scale, the analyte sample has to be delivered from macroscopic world starting with the macro fluidic system. Micro to macro fluidic interfacing block is therefore needed for interconnecting the two different scales of fluidic systems. The macro fluidic block is made from a transparent acrylic block through which 600-μm-diameter

holes are drilled to form L-shaped bent interconnecting fluidic channels. A total of 6 pairs of holes at the top of the block connect to the microfluidic channels that deliver the analyte to sensor heads. The fluid enters the block through tubings attached to the side of the block and are delivered through the top interconnected holes and leave the sensor heads via another set of top interconnected holes and eventually collected through tubings on the side of the block.

Figure 7-6 demonstrates a device and fluidic system assembly.

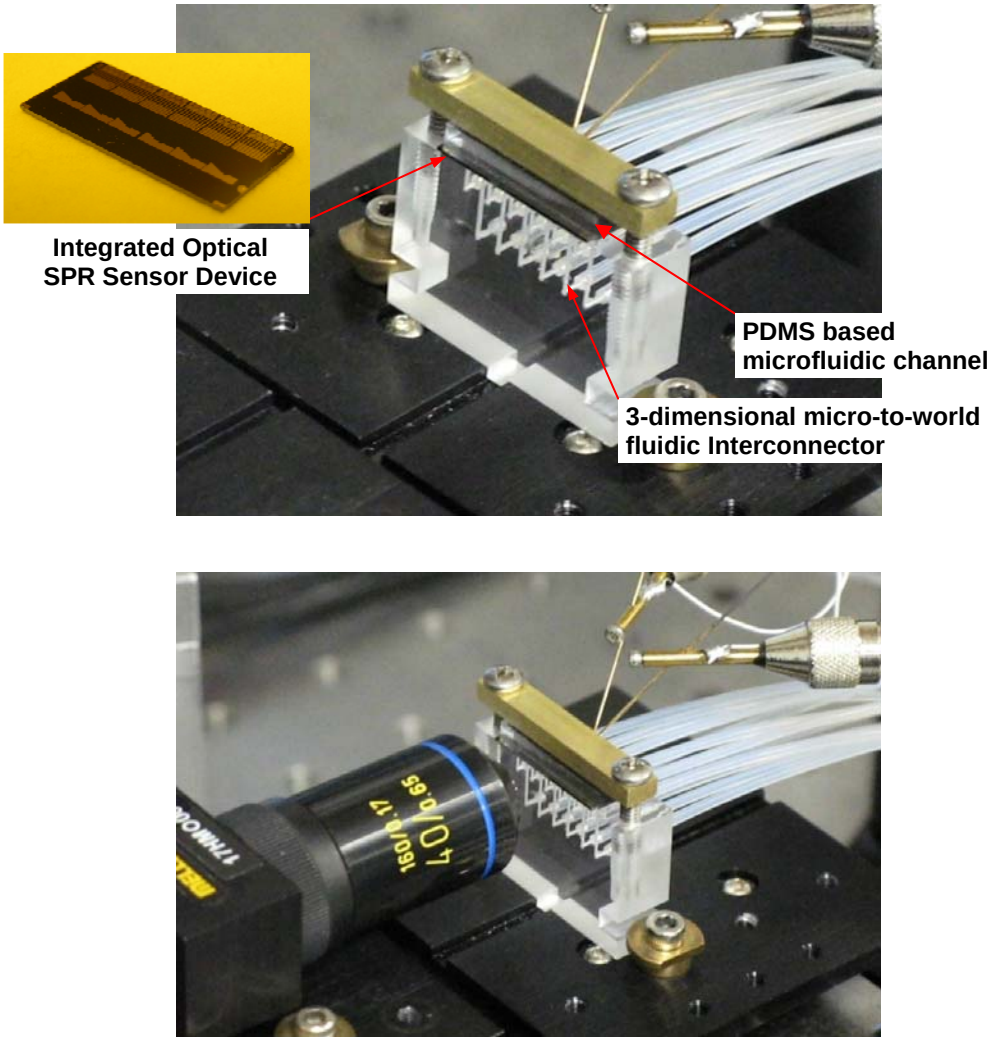

Figure 7-15 Micro to Macro Fluidics Interfacing Block

CHAPTER 8 EXPERIENTAL SET UP

One of the most eminent strength of SPR based biomolecular binding event observation is the real time monitoring capability. To achieve the aforementioned characteristics of SPR spectroscopy, the support of an experimental system with suitable specifications is essential. In a biomolecular assay experiment, once the analyte molecules are introduced into sensor surface, which is treated with analyte recognition elements, the binding event begins and the surface characteristics varies with time as the binding continues.

8.1 Experimental Set Up

For the experiment, two set ups were developed. One set up is for characterizing a SPR sensor head by launching white light and provide rough information on the SPR peak position. The other one is for actual SPR experiment with a photodetector incorporated device. A tunable laser incorporated in the experimental set up requires a control program for automatic wavelength scanning and data acquisition.

The experimental set up for finding the SPR peak position is composed of an optical fiber bundle coupled white light source, a light coupling set up, an imaging set up for coupling the output light into a spectrometer for capturing the transmitted spectrum. Fig. 8-1 shows a sketch of the configuration for white light launching and imaging set up.

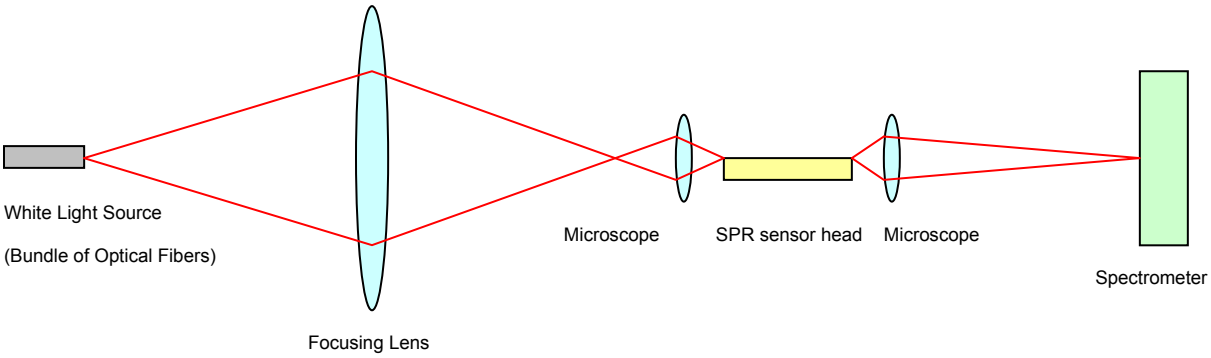

Figure 8-1 White light launching and transmission analysis set up

The experimental set up for wavelength scanning using a tunable laser and spectrum acquisition is developed for the characterization of a photodetector integrated SPR device. To achieve reasonable refractive index variation time resolution, the SPR spectrum scanning and data acquisition procedures need to be fast enough to cope with the speed of the biomolecular binding process. The developed experimental set up is designed to perform spectrum scanning with automatic wavelength control and data acquisition functionalities. Fig. 8-2 shows the operational flow chart of the system.

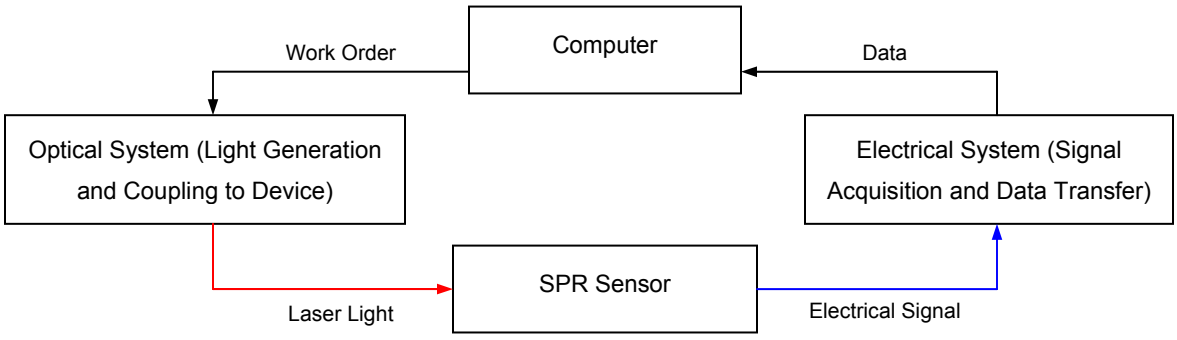

Figure 8-2 SPR Experimental Control and Data Flow

The experimental set up is composed of an optical system which is for light generation, polarization control, and coupling to a device and another set of electronic system for signal acquisition and data transfer. Fig. 8-3 shows the overview of the experimental set up.

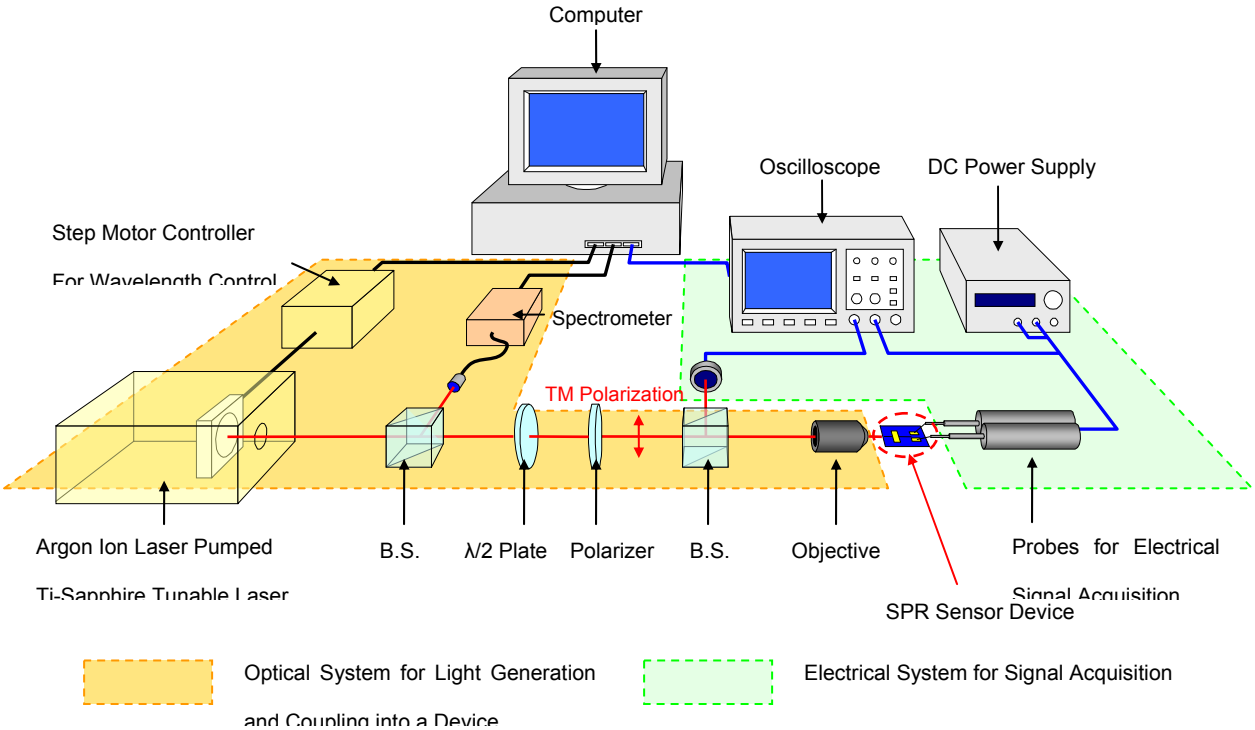

Figure 8-3 SPR Experimental System Over View

8.2 Control Software (wavelength control and data acquisition)

The entire experimental procedure was controlled by a computer using LabVIEW™ which is software control program and provided wavelength control command to a wavelength tuning component in our Ti-sapphire tunable laser and performed the acquisition of the electrical signal data from an interfaced digital oscilloscope. Fig. 8-4 shows the flow chart of the program.

The procedure starts with acquiring parameters; the number of refractive index division, the number of wavelength division, and wavelength tuning crystal angular step corresponding to the wavelength division step. After acquiring the parameters the program is ready to start.

The program is composed of two loops; a small loop for wavelength scanning runs within a large loop for refractive index scan. The loop for wavelength scan starts with tuning a step of wavelength, adding as integer 1 to the variable 'wavelength counter index', and completes by acquiring signal from an oscilloscope and storing the data. This loop iterates until the assigned wavelength range is covered. In the operation, it is assumed that the refractive index of the sample liquid on top of the SPR sensor varies by an amount that is negligible, so that the whole range of wavelength scan applies to one same refractive index.

Once a whole wavelength range is scanned, the system moves the wavelength to the shortest point and restart scanning the wavelength range after a new refractive index sample is placed on the sensor head. The whole number of wavelength scanning is controlled by an index titled 'Refractive index counter index'. When the 'refractive index counter index' equals to the parameter 'number of refractive index steps' the whole procedure finishes. Fig. 8-5 shows the front panel of the control program coded with LabVIEW™.

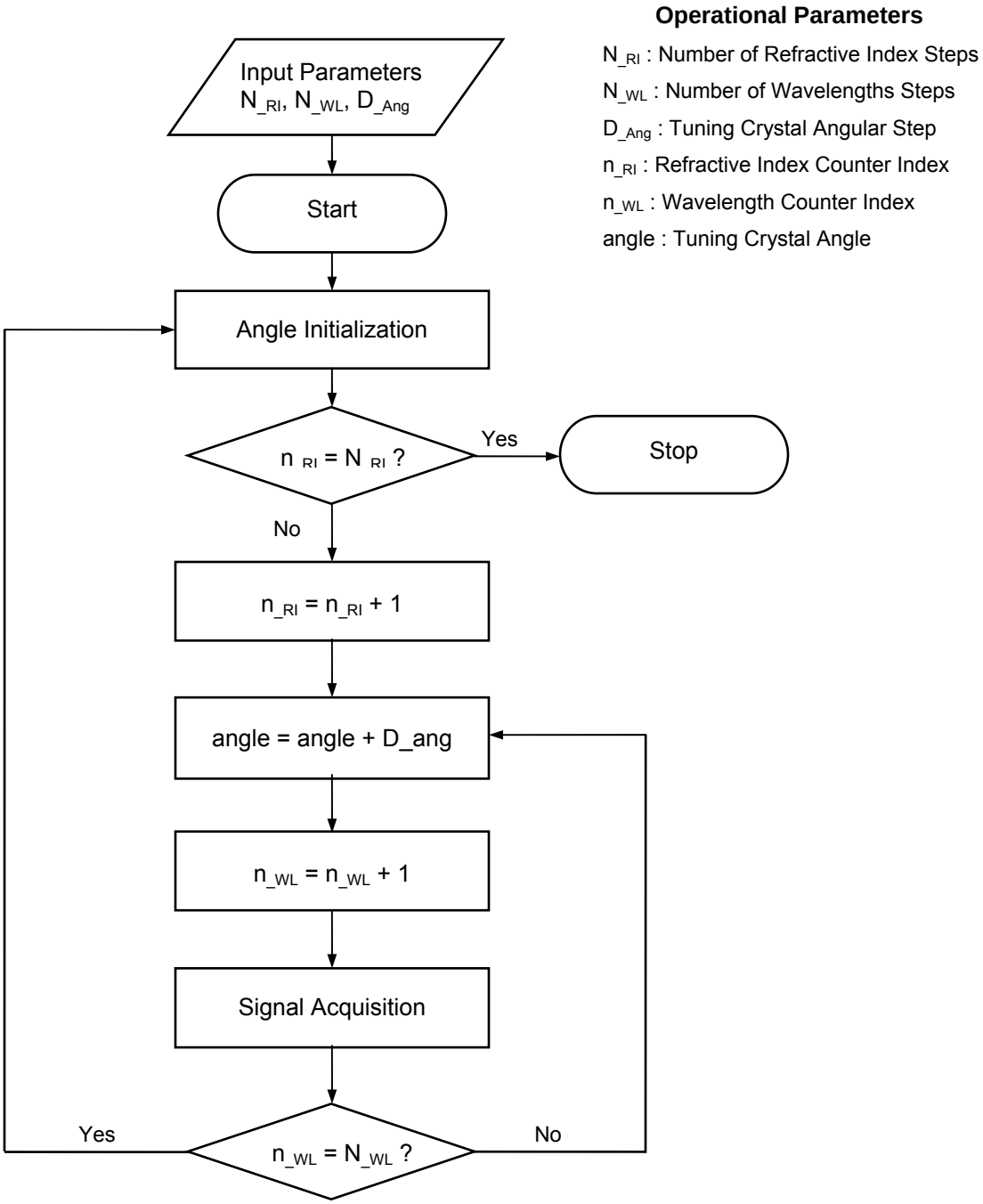

Figure 8-4 Experimental Set Up Block Diagram

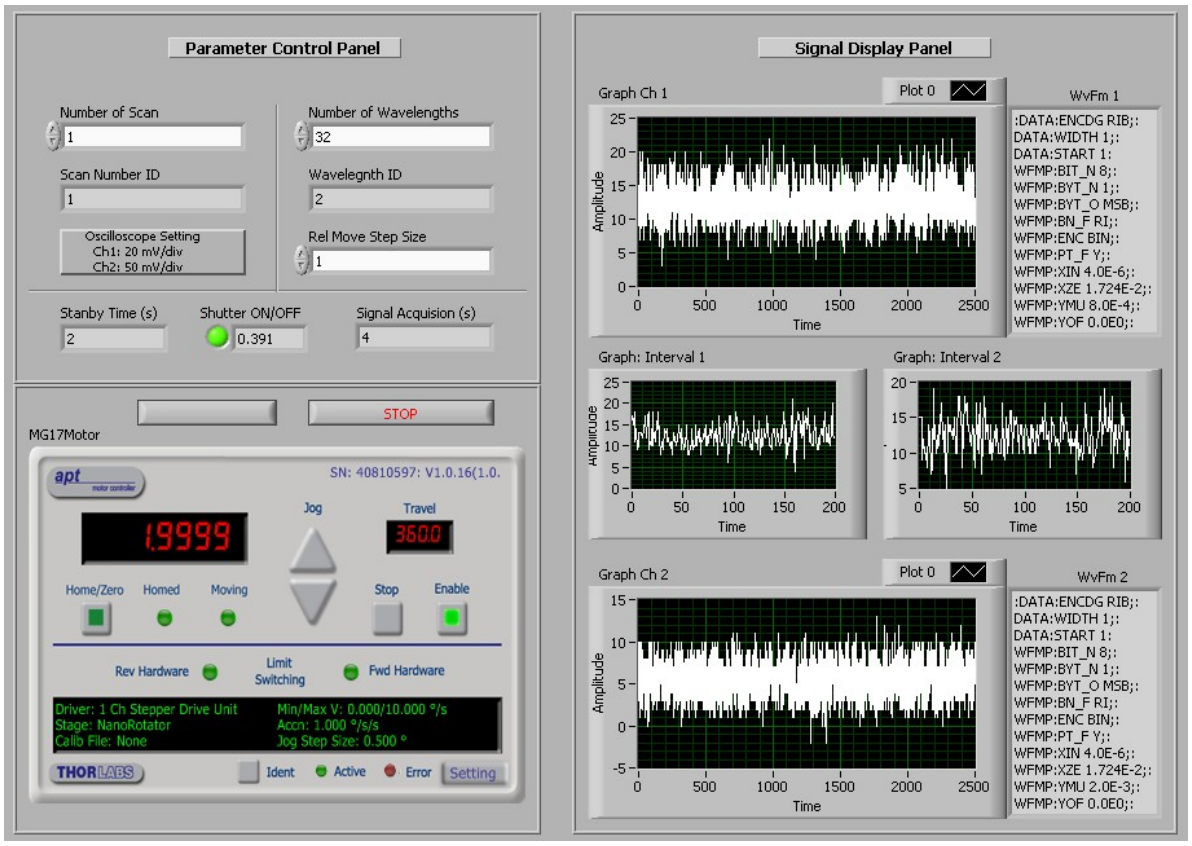

Figure 8-5 Front panel of a program coded with LabVIEW™ for the operation of wavelength control stepper motor and data acquisition from an oscilloscope

8.3 Optical set up for Light Generation and Launching to the Device

The optical set up for the SPR experiment is composed of an Argon ion laser pumped Ti-sapphire tunable laser for light generation, a spectrometer for wavelength information acquisition, a combination of a half wave plate and a polarizer for light polarization/intensity control, a photodetector for reference beam intensity measurement, and a focusing set up for light launching into a device. Figure 8-6 and 8-7 show overview of the optical set up.

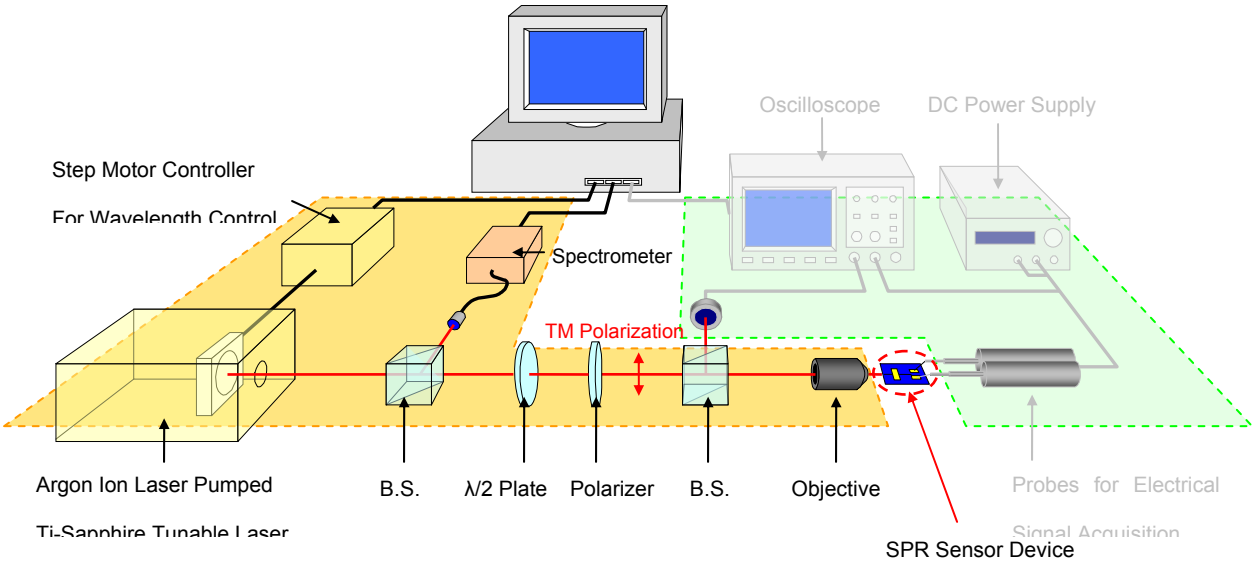

Figure 8-6 Optical set up for SPR experiment

The Ti-sapphire tunable laser is pumped by an Argon-ion laser which generates a beam at a wavelength of 514 nm and 6.7 Watt of power. A birefringent crystal is placed in the Ti-sapphire laser cavity for wavelength tuning. The birefringent crystal is attached to a computer controlled stepper motor so that the wavelength of generated light is set by taking commands from a control computer. A spectrometer (USB4000 Fiber Optic Spectrometer^{TM}, Ocean Optics, Inc.) was used for spectral information acquisition of the transmitted light. The wavelength tuning range of the Ti-sapphire laser that can be achieved using the set of optics and by rotating the birefringent crystal through 30 degrees, is 704 ~ 800 nm.

A combination of a half waveplate and a polarizer converted the laser generated TE polarized mode into TM polarization mode for the excitation of surface plasmon and also served as the light intensity control.

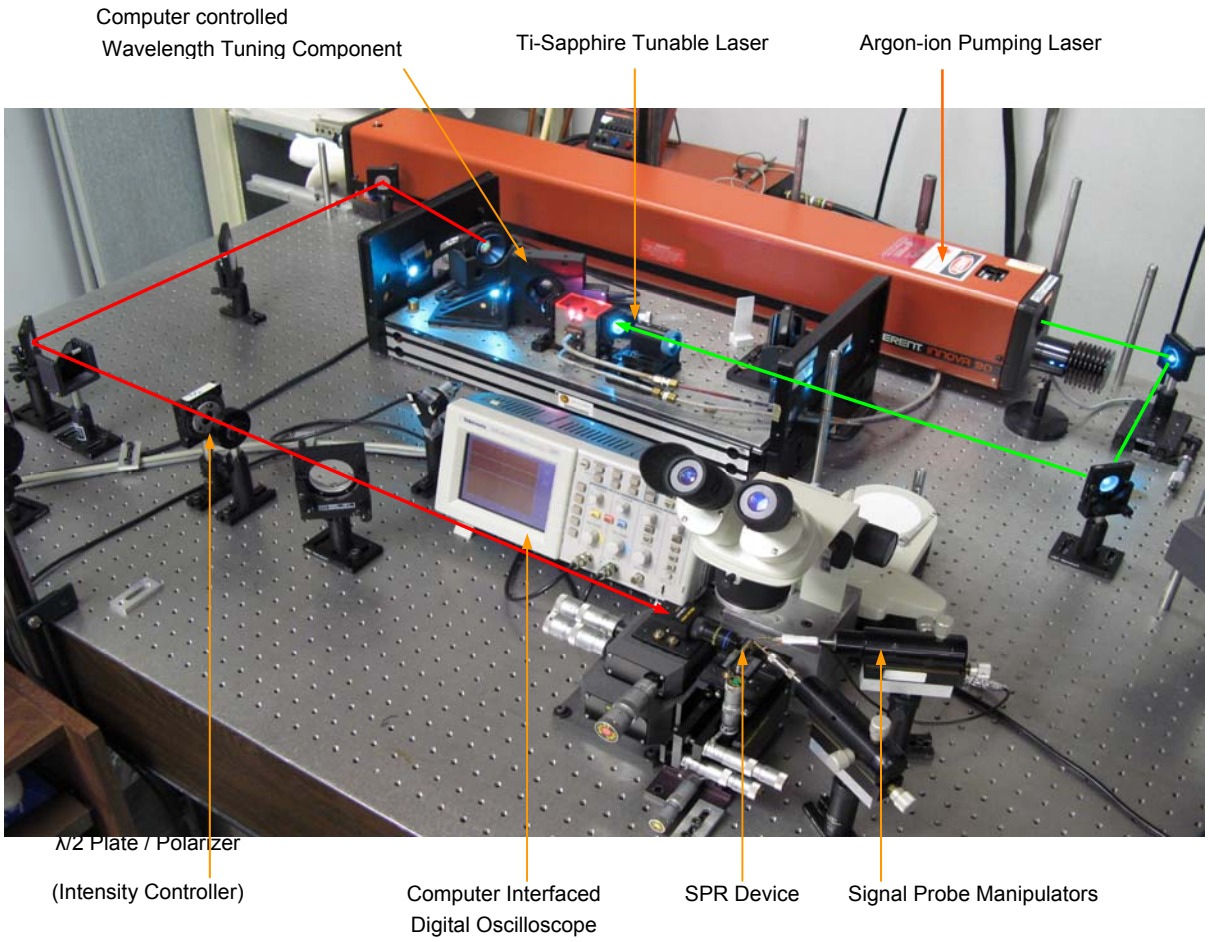

Figure 8-7 Optical Experimental Set Up

Right before coming into the light focusing component the beam was split and coupled to a photodetector (DET100™, Thorlabs, Inc.) for light intensity measurement as a reference signal. A 40x microscope objective lens (Melles Griot, Inc.) mounted on a x-y-z flexure stage (Melles Griot, Inc.) was used for focusing and coupling the laser light into the devices under test.

8.4 Electrical set up for Signal Acquisition

The electrical set up is composed of a probe set up, a DC power supply and an oscilloscope, as shown in Figure 8-8.

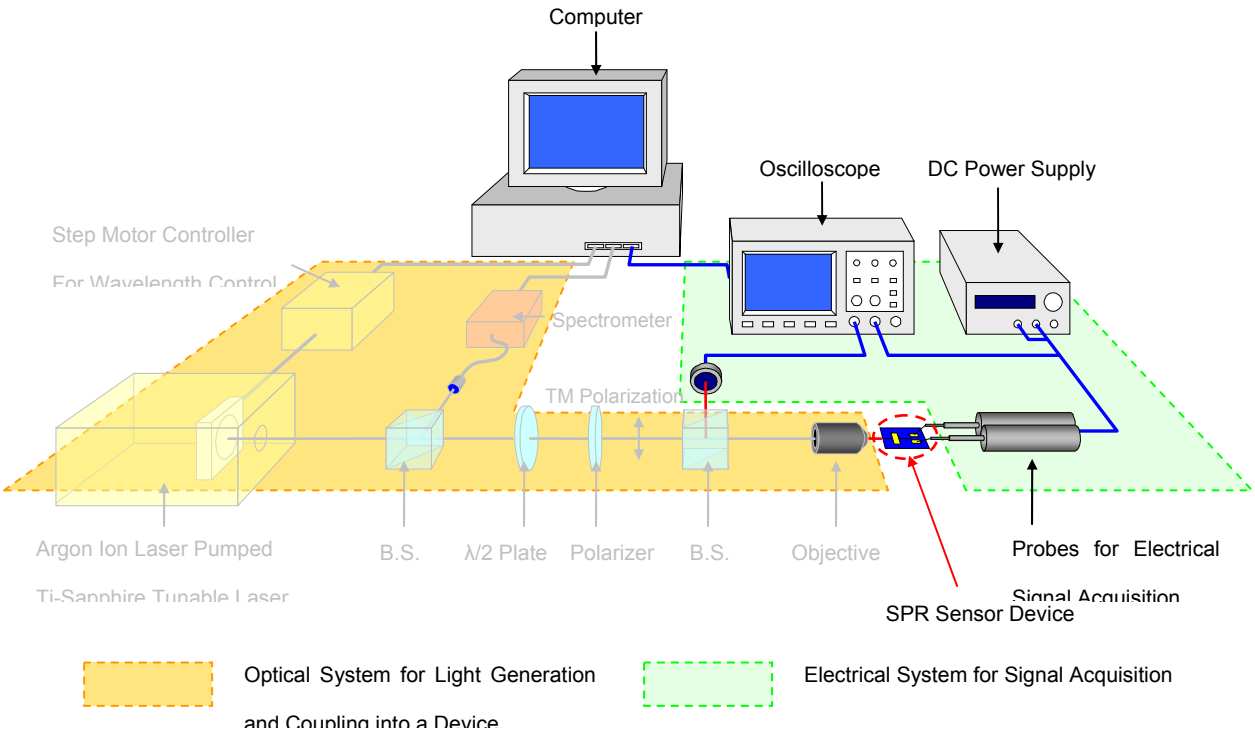

Figure 8-8 Electrical set up for SPR experiment

The probe set up is composed of two micropositioning probes for applying electric current on the substrate integrated photodetector and a serially connected 12 kΩ resistor. DC power supply applies 3 V of DC bias voltage on the resistor. The oscilloscope measures a voltage formed across the resistor. If light is coupled to the integrated MSM photodetector, more current will flow between photodetector's two electrodes and it will be monitored by an increased voltage on the resistor in the probe circuit. The oscilloscope is interfaced via LabView^{TM} to a computer that stores the measured voltages.

CHAPTER 9 EXPERIMENTAL

9.1 Resonance Refractive Index Calculation

Before starting the SPR experiment, a quick calculation is made to estimate the refractive index of the sample solution that will lead to a surface plasmon resonance. The calculation was performed for a wavelength of 740 nm.

Propagation constant of the surface plasmon [39]

$$\beta = \beta' + i\beta'' \approx \frac{\omega}{c}\sqrt{\frac{\varepsilon'_m \cdot \varepsilon_d}{\varepsilon'_m + \varepsilon_d}} + i\frac{\varepsilon''_m}{2(\varepsilon'_m)^2}\frac{\omega}{c}\left(\frac{\varepsilon'_m \cdot \varepsilon_d}{\varepsilon'_m + \varepsilon_d}\right)^{3/2}$$

ε_m : Dielectric constant of metal,

ε_d : Dielectric constant of cover material

$$\beta' = \frac{\omega}{c}\sqrt{\frac{\varepsilon'_m \cdot \varepsilon_d}{\varepsilon'_m + \varepsilon_d}}$$

Refractive index of gold at the wavelength of 740 nm is $\eta = 0.136 + i4.4187$. From the refractive index, real and imaginary part of dielectric constant at the wavelength of 740 nm are calculated to be $\varepsilon_m = \varepsilon'_m + \varepsilon''_m$; $\varepsilon'_m = -19.5064$ and $\varepsilon''_m = 1.2019$ respectively.

The resonance refractive index was calculated with a program coded with LabVIEW™ and the result is as follows. There was a difference between calculated and experimental values. Experimental value for resonance refractive index was 1.524 approximately.

Refractive index of a Sample liquid: 1.4951

• Effective refractive index of the Guided mode: 1.5889523

• Effective refractive index of the Surface Plasmon: 1.58891

9.2 Experimental Procedure

The beam from the Ti-sapphire laser was made to pass through a half-wave plate and a polarizer so that the TM mode could be launched into the waveguide. The light was coupled into the SU-8 guiding layer using a 40x microscope objective lens and the wavelength was scanned from 720 nm to 800 nm. The guided light passes through the SPR sensor head region and the light intensity remaining in the guided mode was measured with the integrated photodetector. As the wavelength of the light was scanned the detected signal decreased as the surface plasmon was being launched. At the wavelength corresponding to the surface plasmon resonance, most of the guided light is converted to surface plasmonic waves and therefore the detected signal is lowest. Therefore the wavelength that corresponds to the lowest detected signal is the SPR wavelength. In order to measure the surface plasmon resonance response, a set of refractive index reference liquids was applied on the SPR sensor head and the transmission spectrum was monitored. The schematic of the wavelength scanning spectrum acquisition experiment is shown in Figure 9-1.

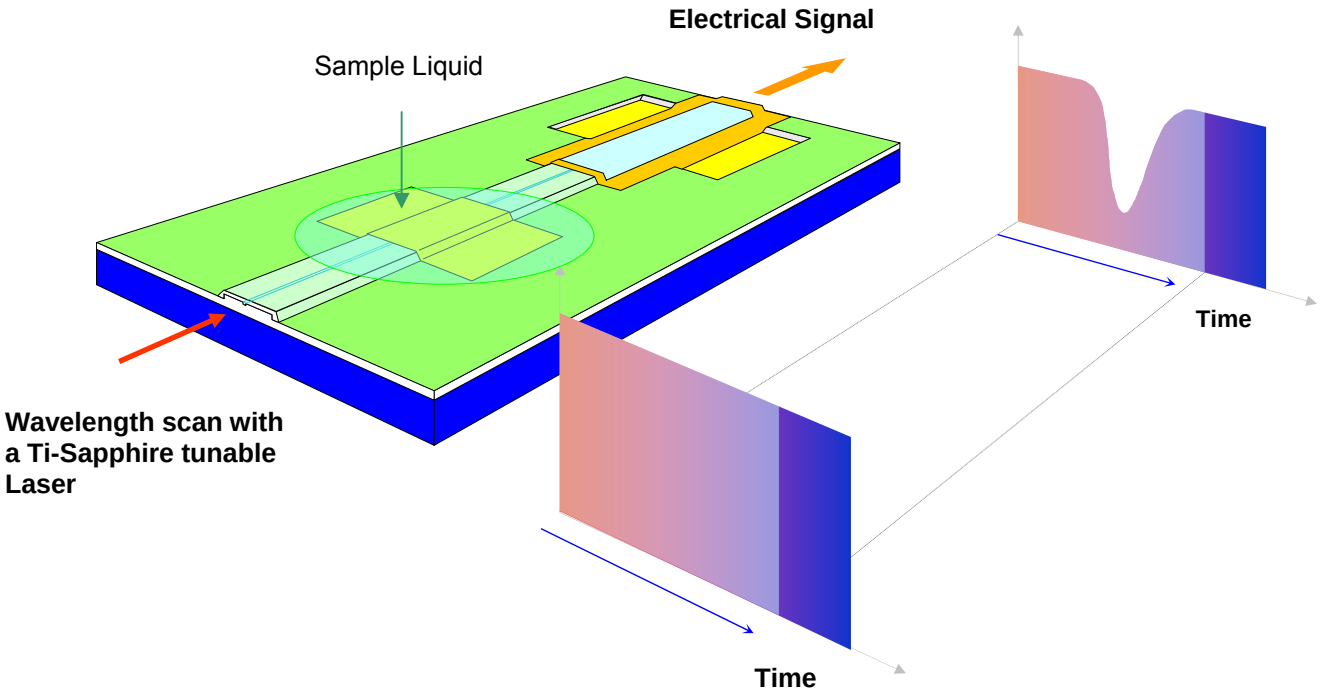

Figure 9-1 Schematic View of SPR Experiment

CHAPTER 10 RESULTS AND DISCUSSION

Transmission spectra were captured for a range of reference refractive index samples in contact with the SPR sensor head. Figure 10-1 (a), (b), and (c) show the transmission spectra obtained with the reference liquids at the refractive indices of 1.520, 1.524, and 1.528, respectively. The shift of the SPR dip position in relation to the refractive index of the reference sample verifies the functionality of our waveguide SPR sensor.

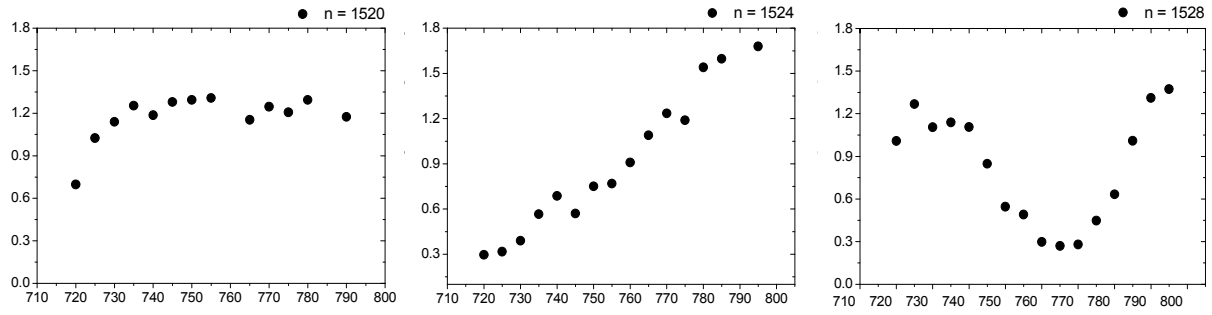

(a) (b) (c)

Figure 10-1 Transmission spectrum depending on refractive index of applied samples
(a) n = 1.520, (b) n = 1.524, and (c) n = 1.528

The position of the dip in the SPR spectrum serves as a measure of the refractive index of sensed medium. Therefore the ability to capture a noise-free SPR spectrum is crucial for biomolecule detection. In this work it is believed that the primary cause of noise originates from the instability of the Ti-sapphire light source. Furthermore, in order to have good sensitivity the SPR dip should be as narrow as possible. The rather broad width of SPR spectrum in our measurement is attributed to either the variations of the waveguide dimension along the beam

propagation direction or an imperfect surface of gold sensor head [40]. Further investigation will to be done to understand the issues and improve the device performance.

CHAPTER 11 CONCLUSION

From this research, a novel mechanism for achieving SPR spectrum was discovered from an integrated optical SPR sensor. Also the functionality of an optoelectronic platform based integrated optical SPR sensor was verified, though some improvement is required to achieve the goal of biomolecular detection.

In the initial stage of this research, SPR sensor heads were designed based on an approximate simulation. The fabricated and tested SPR sensor was designed from the result of this approximate simulation. After a while, a rigorous simulation on the SPR sensor head was executed based on a Finite Element Method (FEM) based simulation tool. From the rigorous simulation, it was found that a novel phenomenon was involved in the designed sensor head and the SPR spectrum was originated from the phenomenon.

In the approximate simulation, it was assumed that the designed SPR sensor head would work based on a conventional absorption type SPR sensing principle. The surface plasmons on the gold sensor head were supposed be to be excited from a guided mode in the dielectric waveguide underneath of the gold layer, when the wavevector of the surface plasmon and that of dielectric guide mode matches. Surface plasmon resonance point in the transmission spectrum was calculated from this assumption. As discussed through chapter 5 to chapter 10, the fabricated device and experiment, were based on the approximate simulation.

As explained in chapter 4, a rigorous simulation took account the entire structure, a dielectric waveguide covered with a gold layer, for a guided mode analysis. Based on the simulation results, the number of modes and power conversion efficiency of the modes at the sensor head

boundaries were calculated. The simulation showed that another principle is involved in making a dip in a SPR spectrum with this sensor head design, as explained through out in chapter 4.

In the case of a SPR spectrum, which was generated from a real microfabricated integrated optical SPR device, geometrical conditions of each structures in the SPR sensor head can affect to final SPR spectrum. So dimensional fluctuations and surface roughness of the structure needs to be meticulously investigated in each steps of the fabrication to achieve good performance and reliability of the device.

As for the working refractive index issue, the developed sensor works for samples with refractive indices around 1.52. However, in the general case, biomolecules are delivered to the sensor head by an aqueous solution. Therefore the refractive index of the sample will be varying around a refractive index of aqueous solution, 1.33, and depending on the biomolecular binding event.

According to our calculations, although the wavevector can be modified depending on the waveguide structure and dimensions, the required amount of wavevector shift cannot to be achieved solely by changing the geometrical parameters of the waveguide with current refractive indices of dielectric waveguide. Therefore lower refractive index materials need to be used for the waveguide fabrication to shift the working refractive index in a future work.

APPENDIX A. FABRICATION PROCESS: SLOPE PATTERNING

A fabrication step for patterning a gentle slope with a simple binary mask was developed, which has been used for giving gentle variations to cladding layer thickness. Figure A.1 (a) and (b) demonstrate sloped patterns on a siliconoxynitride layer made by the developed process. Figure A.2 demonstrates the fabrication process.

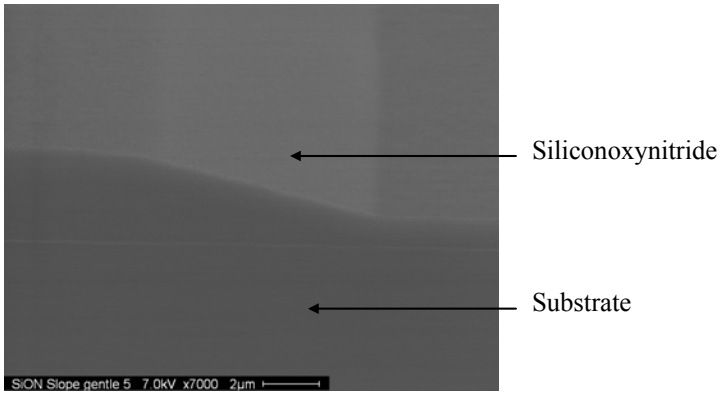

(a)

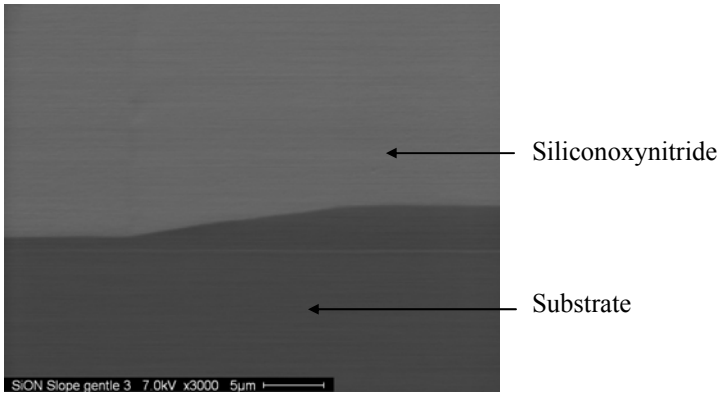

(b)

Figure A.1 SEM image of sloped siliconoxynitride patternsat different locations (a) and (b)

The slope patterning on a siliconoxynitride layer was performed with a sloped NR7-3000PY photoresist patterning and reactive ion etching (RIE) process. Figure A.3 demonstrates the patterning procedure.

1. NR7-3000PY photoresist coating on a siliconoxynitride layer

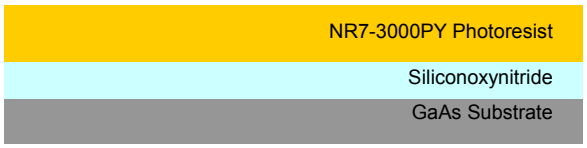

2. UV light exposure with a binary mask lifted to make a gap between the mask and photoresist.

3. Develop the photoresist with RD6 developer.

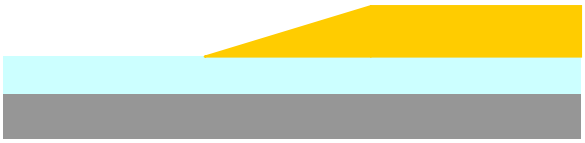

4. RIE etching procedure with the patterned photoresis as an etching mask.

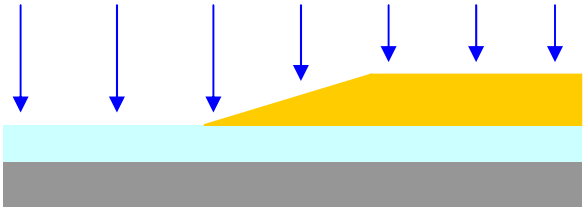

5. Patterned siliconoxynitride with a gentle lope

Figure A.2 Slope patterning with RIE process

APPENDEX B. DEVICE IDENTIFICATION CODE

An array of SPR devices has been fabricated. Figure B.1 demonstrates device identification codes.

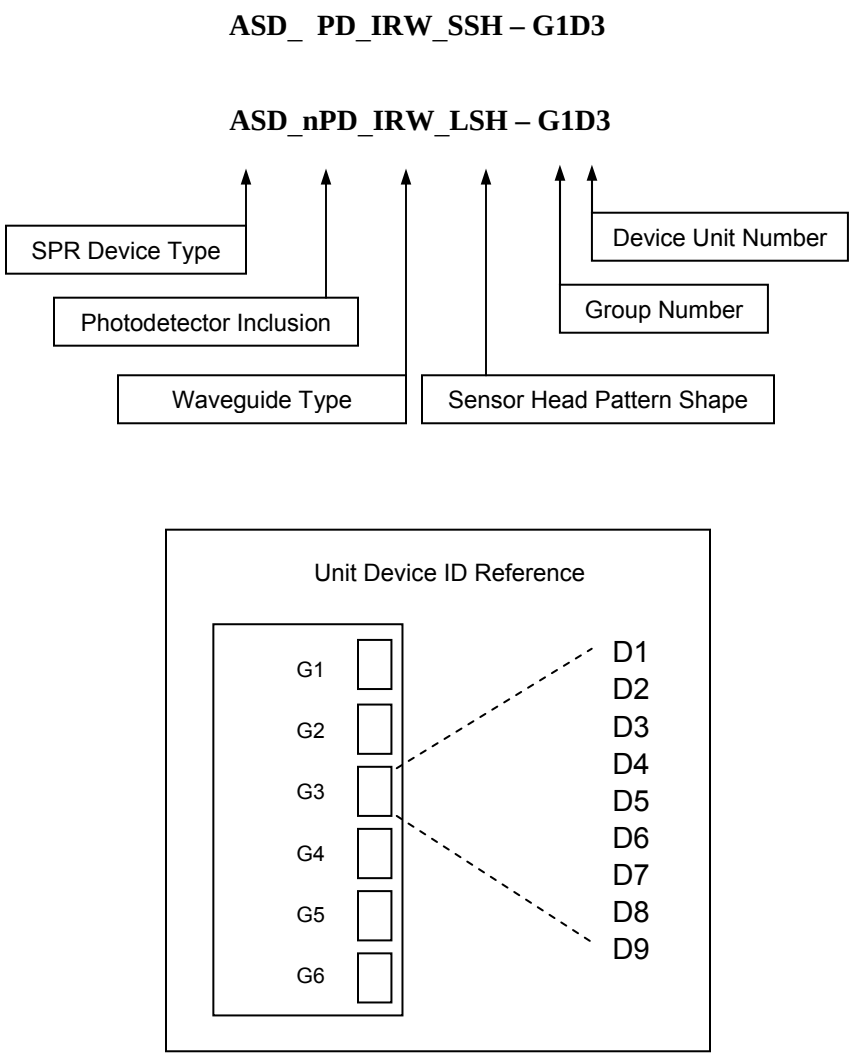

Figure B.1

REFERENCES

[1] L. G. Carrascosa, M. Moreno, M. Alvarez, and L. M. Lechuga, "Nanomechanical biosensors: a new sensing tool," *Trac-Trends in Analytical Chemistry*, vol. 25, pp. 196-206, 2006.

[2] K. Misiakos, S. E. Kakabakos, P. S. Petrou, and H. H. Ruf, "A monolithic silicon optoelectronic transducer as a real-time affinity biosensor," *Analytical Chemistry*, vol. 76, pp. 1366-1373, 2004.

[3] B. J. Luff, R. D. Harris, J. S. Wilkinson, R. Wilson, and D. J. Schiffrin, "Integrated-optical directional coupler biosensor," *Optics Letters*, vol. 21, pp. 618-620, 1996.

[4] H. Y. Quan and Z. X. Guo, "Simulation of whispering-gallery-mode resonance shifts for optical miniature biosensors (vol 93, pg 231, 2006)," *Journal of Quantitative Spectroscopy & Radiative Transfer*, vol. 97, pp. 160-160, 2006.

[5] F. Prieto, A. Llobera, D. Jimenez, C. Domenguez, A. Calle, and L. M. Lechuga, "Design and analysis of silicon antiresonant reflecting optical waveguides for evanscent field sensor," *Journal of Lightwave Technology*, vol. 18, pp. 966-972, 2000.

[6] D. A. Cohen, E. J. Skogen, H. Marchand, and L. A. Coldren, "Monolithic chemical sensor using heterodyned sampled grating DBR lasers," *Electronics Letters*, vol. 37, pp. 1358-1360, 2001.

[7] R. G. Heideman and P. V. Lambeck, "Remote opto-chemical sensing with extreme sensitivity: design, fabrication and performance of a pigtailed integrated optical phase-modulated Mach-Zehnder interferometer system," *Sensors and Actuators B-Chemical*, vol. 61, pp. 100-127, 1999.

[8] K. R. Kribich, R. Copperwhite, H. Barry, B. Kolodziejczyk, J. M. Sabattie, K. O'Dwyer, and B. D. MacCraith, "Novel chemical sensor/biosensor platform based on optical

multimode interference (MMI) couplers," *Sensors and Actuators B-Chemical*, vol. 107, pp. 188-192, 2005.

[9] M. A. Kumar, R. S. Chouhan, M. S. Thakur, B. E. A. Rani, B. Mattiasson, and N. G. Karanth, "Automated flow enzyme-linked immunosorbent assay (ELISA) system for analysis of methyl parathion," *Analytica Chimica Acta*, vol. 560, pp. 30-34, 2006.

[10] U. Lehmann, S. Hadjidj, V. K. Parashar, C. Vandevyver, A. Rida, and M. A. M. Gijs, "Two-dimensional magnetic manipulation of microdroplets on a chip as a platform for bioanalytical applications," *Sensors and Actuators B-Chemical*, vol. 117, pp. 457-463, 2006.

[11] P. Pfeifer, U. Aldinger, G. Schwotzer, S. Diekmann, and P. Steinrucke, "Real time sensing of specific molecular binding using surface plasmon resonance spectroscopy," *Sensors and Actuators B-Chemical*, vol. 54, pp. 166-175, 1999.

[12] A. Suzuki, J. Kondoh, Y. Matsui, S. Shiokawa, and K. Suzuki, "Development of novel optical waveguide surface plasmon resonance (SPR) sensor with dual light emitting diodes," *Sensors and Actuators B-Chemical*, vol. 106, pp. 383-387, 2005.

[13] J. Dostalek, H. Vaisocherova, and J. Homola, "Multichannel surface plasmon resonance biosensor with wavelength division multiplexing," *Sensors and Actuators B-Chemical*, vol. 108, pp. 758-764, 2005.

[14] J. Homola, H. B. B. Lu, G. G. Nenninger, J. Dostalek, and S. S. Yee, "A novel multichannel surface plasmon resonance biosensor," *Sensors and Actuators B-Chemical*, vol. 76, pp. 403-410, 2001.

[15] J. G. Huang, C. L. Lee, H. M. Lin, T. L. Chuang, W. S. Wang, R. H. Juang, C. H. Wang, C. K. Lee, S. M. Lin, and C. W. Lin, "A miniaturized germanium-doped silicon dioxide-based surface plasmon resonance waveguide sensor for immunoassay detection," *Biosensors & Bioelectronics*, vol. 22, pp. 519-525, 2006.

[16] J. Homola, "Present and future of surface plasmon resonance biosensors," *Analytical and Bioanalytical Chemistry*, vol. 377, pp. 528-539, 2003.

[17] P. Tobiska, O. Hugon, A. Trouillet, and H. Gagnaire, "An integrated optic hydrogen sensor based on SPR on palladium," *Sensors and Actuators B-Chemical*, vol. 74, pp. 168-172, 2001.

[18] J. Ctyroky, J. Homola, P. V. Lambeck, S. Musa, H. J. W. M. Hoekstra, R. D. Harris, J. S. Wilkinson, B. Usievich, and N. M. Lyndin, "Theory and modelling of optical waveguide sensors utilising surface plasmon resonance," *Sensors and Actuators B-Chemical*, vol. 54, pp. 66-73, 1999.

[19] R. D. Harris, B. J. Luff, J. S. Wilkinson, J. Piehler, A. Brecht, G. Gauglitz, and R. A. Abuknesha, "Integrated optical surface plasmon resonance immunoprobe for simazine detection," *Biosensors & Bioelectronics*, vol. 14, pp. 377-386, 1999.

[20] J. Dostalek, J. Ctyroky, J. Homola, E. Brynda, M. Skalsky, P. Nekvindova, J. Spirkova, J. Skvor, and J. Schrofel, "Surface plasmon resonance biosensor based on integrated optical waveguide," *Sensors and Actuators B-Chemical*, vol. 76, pp. 8-12, 2001.

[21] A. R. Wheeler, S. Chah, R. J. Whelan, and R. N. Zare, "Poly(dimethylsiloxane) microfluidic flow cells for surface plasmon resonance spectroscopy," *Sensors and Actuators B-Chemical*, vol. 98, pp. 208-214, 2004.

[22] J. Spadavecchia, M. G. Manera, F. Quaranta, P. Siciliano, and R. Rella, "Surface plamon resonance imaging of DNA based biosensors for potential applications in food analysis," *Biosensors & Bioelectronics*, vol. 21, pp. 894-900, 2005.

[23] T. J. Wang, W. S. Lin, and F. K. Liu, "Integrated-optic biosensor by electro-optically modulated surface plasmon resonance," *Biosensors & Bioelectronics*, vol. 22, pp. 1441-1446, 2007.

[24] J. Ctyroky, J. Homola, and M. Skalsky, "Tuning of spectral operation range of a waveguide surface plasmon resonance sensor," *Electronics Letters*, vol. 33, pp. 1246-1248, 1997.

[25] T. A. Anhoj, A. M. Jorgensen, D. A. Zauner, and J. Hubner, "The effect of soft bake temperature on the polymerization of SU-8 photoresist," *Journal of Micromechanics and Microengineering*, vol. 16, pp. 1819-1824, 2006.

[26] J. Boudiombo, A. Boudrioua, J. C. Loulergue, S. Malhouitre, and J. Machet, "Optical waveguiding properties and refractive index analysis of boron nitride (BN) thin films prepared by reactive ion plating," *Optical Materials*, vol. 10, pp. 143-153, 1998.

[27] P. Bindner, A. Boudrioua, P. Moretti, and J. C. Loulergue, "Refractive index behaviors of helium implanted optical planar waveguides in LiNbO3, KTiOPO4 and Li2B4O7," *Nuclear Instruments & Methods in Physics Research Section B-Beam Interactions with Materials and Atoms*, vol. 142, pp. 329-337, 1998.

[28] M. Modreanu and M. Gartner, "Investigation on optical properties of CVD films used in MOEMS applications," *Journal of Molecular Structure*, vol. 565, pp. 519-523, 2001.

[29] R. M. de Ridder, K. Worhoff, A. Driessen, P. V. Lambeck, and H. Albers, "Silicon oxynitride planar waveguiding structures for application in optical communication," *Ieee Journal of Selected Topics in Quantum Electronics*, vol. 4, pp. 930-937, 1998.

[30] O. Buiu, G. P. Kennedy, M. Gartner, and S. Taylor, "Structural analysis of silicon dioxide and silicon oxynitride films produced using an oxygen plasma," *Ieee Transactions on Plasma Science*, vol. 26, pp. 1700-1712, 1998.

[31] D. Criado, I. Pereyra, and M. I. Alayo, "Study of nitrogen-rich silicon oxynitride films obtained by PECVD," *Materials Characterization*, vol. 50, pp. 167-171, 2003.

[32] A. Aboudou, E. Goutain, J. P. Vilcot, M. Francois, L. Joannes, and D. Decoster, "Monolithic Integration of Gaas Msm Photodetector and Sio2/Si3n4 Dielectric Optical Wave-Guide," *Electronics Letters*, vol. 28, pp. 52-53, 1992.

[33] M. Siegert, M. Loken, C. Glingener, and C. Buchal, "Efficient optical coupling between a polymeric waveguide and an ultrafast silicon MSM photodiode," *Ieee Journal of Selected Topics in Quantum Electronics*, vol. 4, pp. 970-974, 1998.

[34] D. Zurhelle, O. Blume, S. Popp, and J. Muller, "Highly efficient waveguide-detector coupling structures for integrated opto-electronical circuits on silicon," *Journal of Lightwave Technology*, vol. 14, pp. 410-416, 1996.

[35] C. L. Callender, L. Robitaille, J. P. Noad, F. Gouin, and C. A. Almeida, "Optical signal distribution to MSM photodetector arrays via integrated polyimide waveguides," *Journal of Lightwave Technology*, vol. 15, pp. 1700-1707, 1997.

[36] T. Tanimoto, I. Ohbu, H. Ohta, and S. Takatani, "Reduction of Schottky reverse leakage current using GaAs surface cleaning with UVO3 treatment," *Japanese Journal of Applied Physics Part 1-Regular Papers Short Notes & Review Papers*, vol. 38, pp. 3982-3985, 1999.

[37] W. C. Koscielniak, J. L. Pelouard, R. M. Kolbas, and M. A. Littlejohn, "Dark Current Characteristics of Gaas Metal-Semiconductor Metal (Msm) Photodetectors," *Ieee Transactions on Electron Devices*, vol. 37, pp. 1623-1629, 1990.

[38] W. A. Wohlmuth, P. Fay, and I. Adesida, "Dark current suppression in GaAs metal-semiconductor-metal photodetectors," *Ieee Photonics Technology Letters*, vol. 8, pp. 1061-1063, 1996.

[39] P. Adam, J. Dostalek, and J. Homola, "Multiple surface plasmon spectroscopy for study of biomolecular systems," *Sensors and Actuators B-Chemical*, vol. 113, pp. 774-781, 2006.

[40] T. Akimoto, S. Sasaki, K. Ikebukuro, and I. Karube, "Refractive-index and thickness sensitivity in surface plasmon resonance spectroscopy," *Applied Optics*, vol. 38, pp. 4058-4064, 1999.